ALMA MATER STUDIORUM
UNIVERSITÀ DI BOLOGNA

DOTTORATO DI RICERCA IN

INGEGNERIA BIOMEDICA, ELETTRICA E DEI SISTEMI

Ciclo 38

Settore Concorsuale: 09/E4 - MISURE

Settore Scientifico Disciplinare: ING-INF/07 - MISURE ELETTRICHE E ELETTRONICHE

MODELLING AND CHARACTERIZATION OF LOW-POWER CURRENT TRANSFORMERS FOR THE CHALLENGES OF MODERN POWER NETWORKS

Presentata da: Christian Betti

Coordinatore Dottorato

Michele Monaci

Supervisore

Alessandro Mingotti

Co-supervisore

Lorenzo Peretto

Esame finale anno 2026

Abstract

This doctoral thesis presents the main activities and results obtained over three years of research dedicated to developing and validating novel, simplified and cost-effective metrological characterization procedures for Medium Voltage (MV) Low-Power Current Transformers (LPCTs).

In recent years, the power grid has undergone drastic changes. The widespread integration of Renewable Energy Sources (RESs) and the consequent deployment of switching power converters are among the primary causes of harmonic injection into modern smart grids, with a significant impact on Power Quality (PQ) levels. However, legacy inductive Instrument Transformers (ITs) are not a reliable solution for performing accurate PQ monitoring. In this scenario, new technologies have been developed to fill this gap, and Low-Power Instrument Transformers (LPITs) have emerged as a promising solution thanks to advantages such as a superior linear frequency response and many others. Nevertheless, these new transducers suffer from some critical issues, including sensitivity to external quantities such as temperature and electromagnetic fields. Therefore, this thesis addresses the challenge of developing simplified procedures for accurately measuring the frequency response of LPITs in the PQ frequency range under predefined working conditions.

In this work, the proposed techniques target industry stakeholders, from Distribution System Operators (DSOs) to small technical offices, aiming to reduce costs, simplify procedures, shorten operational working times, while also providing a further contribution to the scientific community.

The thesis is organized as follows. Two introductory chapters present the background necessary to understand the significance of the research. First, Chapter 1 discusses the characteristics of current sensors and transducers installed in modern power systems, providing a comprehensive overview of the standards that regulate them. Then, Chapter 2 summarizes the practices and methods used to calculate the mea-

surement uncertainty associated with a measurement result.
Subsequently, Chapter 3 represents the original contributions, which are divided into three parts. The first section validates a new and straightforward method for obtaining the frequency model of commercial Rogowski Coils (RCs) based on input data taken from the device data-sheet. Validation is performed through both simulation and experimental data. The second section experimentally investigates the variability of the output of identical RCs subjected to the same working conditions. The third and final section develops a simplified characterization procedure for the RCs frequency response, and its results are compared with those acquired using a traditional method.

Contents

Chapter 1

Overview of Medium Voltage Sensors for Current Measurements

In recent years, the modern power network has undergone a drastic transformation, mainly caused by: (i) the integration of RESs such as Photovoltaic (PV) plants [1, 2], (ii) the trend towards the electrification of many sectors –such as the proliferation of Electric Vehicle (EV) [3], heating and cooling of buildings [4], industrial processes and several other sectors–, (iii) grid digitalisation and development of smart grids [5] and (iv) decentralized production and consumption. This change is driven by international bodies seeking to reduce the power system's impact on climate and natural resources [6]. Due to this evolution, traditional monitoring and controlling techniques have become obsolete, urging the need for new and more advanced solutions –also based on Machine Learning (ML) [7, 8] and Artificial Intelligence (AI) [9]– in order to monitor the health of these electrical grid assets in real-time and consequently prevent or minimize the effect of failures, instabilities, power outages and contingencies. Therefore, to address the challenges introduced by this new scenario and in particular improve its observability, high-quality data from distributed measurement are needed [10]. The consequence is a massive increase in the number of measuring points where sensors and Intelligent Electronic Devices (IEDs) measure and process electrical quantities in the most accurate way. In conclusion, the field of instrumentation and electrical measurement plays a key role in ensuring the reliability, stability and efficiency of the modern grid. Voltages and currents at nodes, branches and assets are the main quantities measured to accurately evaluate the health status of MV and High Voltage (HV)power networks. This type of electrical measurement is the responsibility of ITs because they provide accurate measurements of voltage and current across a wide range of operating conditions. In fact, ITs deliver scaled signals for control, protection, and metering purposes that are at a suitable level to be safely acquired by Data Acquisition (DAQ) systems. Due to their importance, researchers have produced a vast amount of literature and the International Electrotechnical Commission (IEC) has created a dedicated Technical Committee (TC) –TC38– and a family of standards –61869– that regulates every aspect of ITs.

The present chapter reviews the Current Transformers (CTs) used during the PhD programme, focusing in particular on RCs. Then, it provides an outlook on ITs standards.

1.1 Inductive Current Transformers

Although LPCTs are increasingly replacing traditional inductive ITs, a brief description of the foundational principles of IT is needed.

The basic structure of an inductive transformer includes a magnetic core, usually built from thin metal layers, and two copper windings: the primary and the secondary. Such structure is represented in figure 1.1.

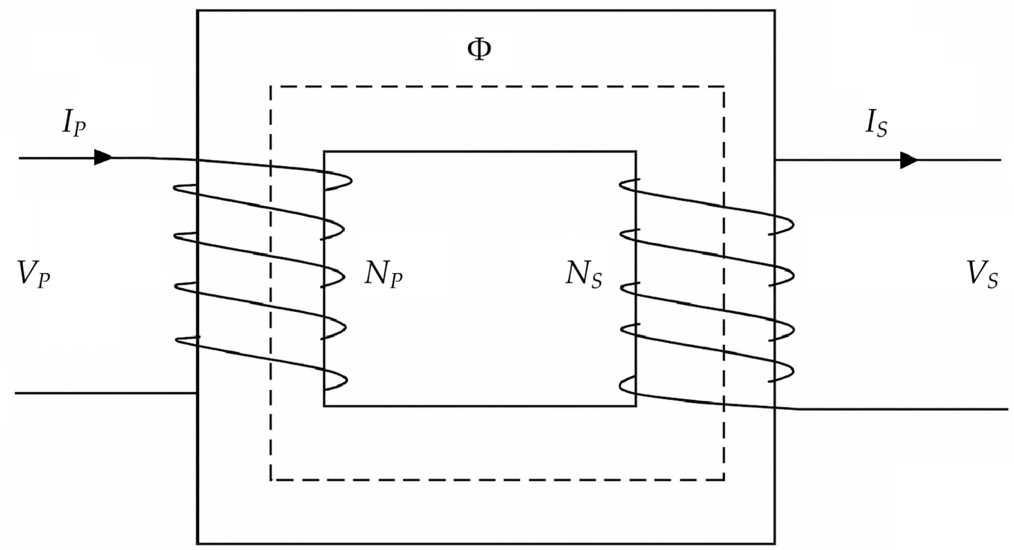

Figure 1.1: Main components of a generic transformer.

Therefore, for an ideal transformer, the relationships between primary and secondary voltages (V), currents (I), and turn counts (N) are:

$$\frac{V_P}{V_S} = \frac{N_P}{N_S} = \frac{I_S}{I_P}, \tag{1.1}$$

where: (i) V_P and V_S are the rms values of the primary and secondary voltages, respectively, (ii) N_P and N_S are the number of turns of the primary and secondary, respectively, and (iii) I_P and I_S are the rms values of the primary and secondary currents, respectively. Equation (1.1) assumes an ideal magnetic core (no losses, infinite permeability) and perfectly coupled windings. Therefore, the input-output relationship of the ideal transformer is linear. However, real transformers deviate greatly from the ideal model. A more accurate representation includes the series (longitudinal) parameters on both the primary and secondary sides and a shunt (transversal) branch on the primary side (see figure 1.2). In the usual notation:

$$Z_1 = R_1 + jX_1, \tag{1.2}$$

$$Z_2 = R_2 + jX_2, \tag{1.3}$$

$$Y_0 = \frac{1}{R_0} + j\frac{1}{X_0}, \tag{1.4}$$

where:

- R_1 and R_2 are the copper (Joule) loss resistances of the primary and secondary windings;
- X_1 and X_2 are the leakage reactances accounting for the leakage (dispersed) magnetic flux not linking both windings;
- R_0 models core losses (primarily hysteresis and eddy-current losses);
- X_0 is the magnetizing reactance (often expressed as $X_0 = \omega L_m$, with L_m the magnetizing inductance).

The shunt branch Y_0 captures excitation phenomena in the core, while Z_1 and Z_2 collect the distributed series effects of the windings. All quantities may be referred to one side of the transformer for analysis. Taking these new parameters into account, the input-output relationship of the real transformer is no longer linear. Finally, this equivalent model is valid for every transformer –instrument and power transformers.

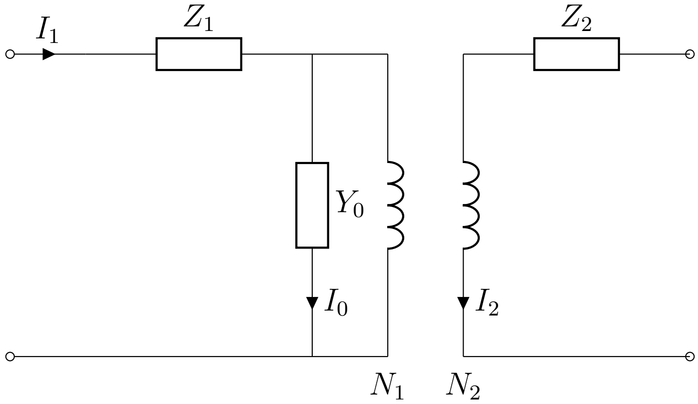

Figure 1.2: Transformer equivalent circuit.

Shifting the focus to CTs, such devices, like inductive Voltage Transformer (VT), consist of primary and secondary windings wound around a ferromagnetic core. However, unlike VT, the number of turns in the primary coil is small as the measurement objective is to reduce the current to be measured, so that $I_2 < I_1$ and, accordingly, $N_1 < N_2$. In some cases, the primary is just a single winding –the conductor whose current flowing through it has to be measured–, therefore $N_1 = 1$. In the latter case, typical for Low Voltage (LV) systems, the CT employs a toroidal ferromagnetic core on which only the secondary is wound, while the primary conductor passes straight through the core aperture. In practical application, three main types of CT can be distinguished: wound-type, bar-type, and toroidal-type. The wound-type and the bar-type have to be installed in series to the main circuit resulting in interruption of the service. The latter is a single turn configuration. On the contrary, the toroidal-type requires that the primary conductor be inserted into the CT hole.

As for the installation of CTs, taking into consideration figure 1.4, the primary winding is installed in series with the current to be measured, while the secondary is closed on a resistive load, called burden. Such burden has to be very low since CT are intended to work with the secondary short-circuited. In fact, if the secondary is accidentally open-circuited, the transformation ratio determines a hazardous induced HV voltage at the secondary which could be destructive for the winding insulation and deadly for human operators. Therefore, an electrical protection is necessary.

In addition, the secondary is connected to earth to discharge any dangerous capacitive currents and thus ensure electrical safety.

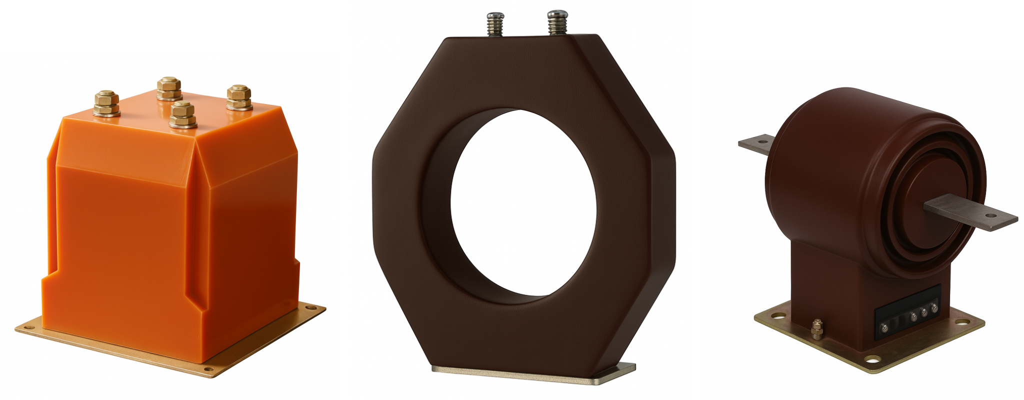

(a) Wound-type current transformer. (b) Toroidal-type current transformer. (c) Bar-type current transformer.

Figure 1.3: Comparison of the different current transformer configurations.

Furthermore, CTs have a limited bandwidth which makes them unusable for PQ measurements due to resonance and saturation problems of the ferromagnetic core.

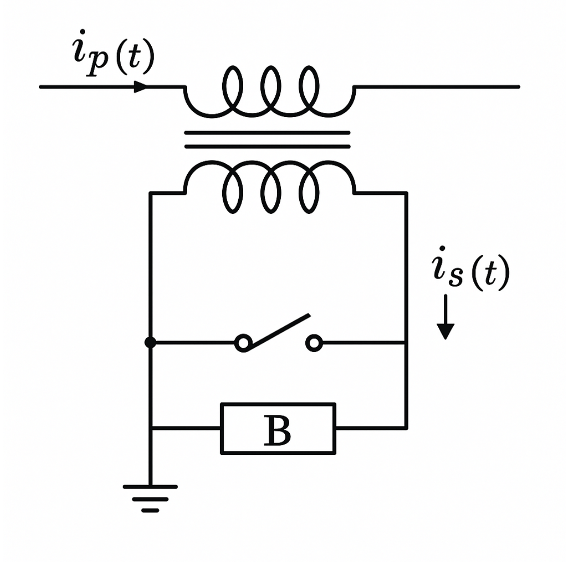

Figure 1.4: Inductive current transformer insertion schematic.

To quantify how much a real transformer deviates from its ideal behavior, the international standards, which will be explored in more detail in section 1.3, propose two accuracy indices –ratio error ε and phase displacement $\Delta\varphi$– thanks to which it is possible to evaluate how accurately the secondary quantities (current or voltage) reflect the primary quantities (to be measured). Obviously, every manufacturer tries to minimize these indices. From [11], ratio error is "the error which an instrument transformer introduces into the measurement and which arises from the fact that the actual transformation ratio is not equal to the rated transformation ratio", whereas the phase displacement is "the difference in phase between the primary voltage or current phasor and the secondary voltage or current phasor, the positive direction of the phasors being so chosen that the phase displacement is zero for an ideal transformer". Finally, ratio error and phase displacement for CTs are defined as:

$$\varepsilon = \frac{k_n I_S - I_P}{I_P} \cdot 100\,, \tag{1.5}$$

$$\Delta\varphi = \hat{I}_S - \hat{I}_P\,, \tag{1.6}$$

where: (i) k_n is the nominal transformation ratio of CT, (ii) I_P and I_S are the rms values of the primary and secondary currents, respectively, and (iii) $\hat{I}_P$ and $\hat{I}_P$ are the phase angles of the primary- and secondary-current phasors. Such indices are used to quantify CT performance.

A final comment on CTs: industrial CTs have a normalized secondary nominal current –usually 1 A, 2 A, or 5 A– to standardize acquisition systems. However, these values are not compatible with almost all modern measurement systems based on DAQ boards, which have a voltage input. Therefore, CTs require an additional device on their output, namely a current transducer.

1.2 Low-power Current Transformers

1.2.1 Rogowski Coils

Nowadays, RCs are one of the most used types of LPCTs for current measurements. Such devices are part of the group of LPCT. They are installed in power systems for measuring Alternating Current (AC) current. RCs are widely adopted due to their advantageous characteristics, which become particularly significant when compared to conventional inductive CTs. For instance, RCs, represented by a sample in figure 1.5, are:

- smaller in size, and therefore they can be installed in small spaces such as small electrical cabinets crowded full of other equipment;

- lighter in weight, not having a ferromagnetic core, and therefore ensuring easier installation by operators;
- cheaper, because they are less heavy and are not made of much metal material;
- structurally openable and flexible and consequently this facilitates the RC installation as the physical connection in series with the conductor is not needed, but it is possible to easily wrap the RC around conductors of various sizes and shapes. In this way, the outage of electrical assets is excluded;
- not affected by magnetic saturation problems as they do not have an iron core, thereby ensuring a wide linear frequency response up to tens of kHz and therefore making this type of transducer suitable for PQ measurements;
- safer, as they are not affected by large overloads or dangerous overvoltages due to the open secondary;
- suitable for being connected to IEDs thanks to the low-power output –below 1 V;
- highly accurate in measuring large current as RC are not affected by magnetic saturation or significant heat generation.

Figure 1.5: Rogowski coil picture.

Thanks to their numerous advantages, RCs are an interesting choice for current measurement in power systems, but their practical use presents some challenges. The installation and calibration processes can be complex, requiring technical expertise, for the following main reasons:

- improperly shielded coils are sensitive to external magnetic fields –usually induced by currents flowing in adjacent phases in three-phase systems;
- the sensor output depends on the ambient temperature;
- the sensor output is also highly dependent on the position of the RC relative to the conductor passing through it;
- output voltage is proportional to the derivative of the measured current according to equation (1.7), and therefore an integration stage is required.

Ambient temperature, external magnetic fields, and relative position of the conductor can be defined as "influence quantities" for RCs. In fact, according to [12], the definition of "influence quantity" is: "quantity that does not affect the quantity being measured but that affects the measurement result". Because these are critical quantities for successful accurate measurement, international standards, such as [13], indicate how the effects of these quantities should be measured.

The structure of RCs is relatively simple and is illustrated in figure 1.6. The RC sensor consists of a metal wire –usually copper– wrapped around an iron-free insulating support. The conductor carrying the unknown primary current, $i_p(t)$, is passed through the coil.

As the operating principle of the RC is based on Faraday's law of induction, the sensor's output is a voltage, $u_s(t)$. Such voltage is directly proportional to the time derivative of the primary current according to the following equation:

$$u_s(t) = -M \frac{\mathrm{d}i_p(t)}{\mathrm{d}t}. \tag{1.7}$$

where M represents the mutual inductance of the coil between the primary conductor and the secondary winding. Appendix A derives equation (1.7).

From the analysis of the equation (1.7) –input-output relationship of the RC– it can be noted that its output, being a voltage, facilitates direct interfacing with Analog to Digital Converters (ADCs), simplifying the measurement chain –no additional

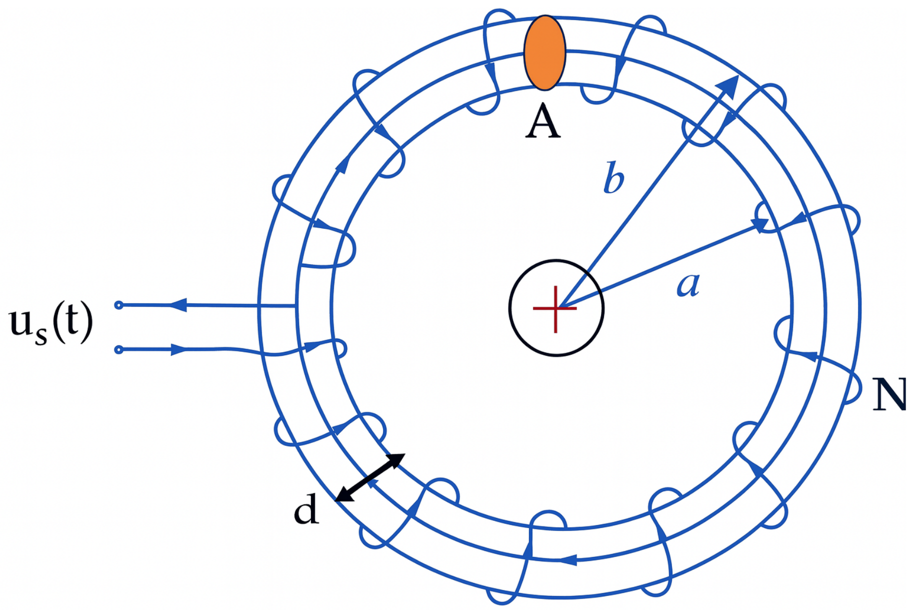

Figure 1.6: Rogowski coil structure.

transducer is required. However, the output signal represents the derivative of the primary current, not the current waveform itself reduced according to a certain transformation ratio. Therefore, to reconstruct the true shape of $i_p(t)$, a subsequent analog or digital integration stage is required. For clarity, it is important to emphasize that the scope of this research is confined to the behavior of the RC itself, ignoring the signal integration system. This approach was adopted because the inclusion of this additional signal processing system would introduce further system variables and complexity into the model of the transducer.

1.3 IEC 61869

After an overview of legacy and low-power CTs, it is important to describe the context of the standards. The family of international standard IEC 61869 provides a comprehensive framework, outlining design specifications, testing procedures, and accuracy evaluation. The IEC TC38 has currently published 13 active standards and 3 technical reports. Table 1.3 lists all these documents.

Until two years ago, the standard [14] was divided into two: [15] and [16], but it was preferred to combine the general requirements of traditional inductive ITs (VTs, CTs and Capacitor Voltage Transformerss (CVTs)) with LPITs (Low-Power Voltage Transformers (LPVTs) and LPCTs). In this way, this first standard became the fundamental norm of this family of standards, prescribing general requirements for all devices, from the oldest to the most modern, covered by 61869 . Among the general aspects regulated, there are: (i) environmental service conditions, (ii) insulation requirements, (iii) Electromagnetic Compatibility (EMC) and (iv) test procedures. At the same time, this structure offers the flexibility needed to quickly integrate new constraints and aspects without having to revise all the standards one by one. Finally, this first standard is complemented by a series of more specific documents depending on the type of transformer or the technology used.

The 61869 series can be logically divided into the following macro-areas:

- conventional inductive transformers (Parts 2, 3, 4, and 5);
- low-power transformers (Parts 7, 8, 10, and 11);
- digital interface and system components (Parts 9 and 13).
- Direct Current (DC) applications (Parts 14 and 15).
- additional requirements and guides (Part 20, Part 99, and Technical Reports).

Currently, the standard [14] applies to ITs intended for applications where the nominal voltage is greater than 1 kV AC or 1.5 kV direct current DC, therefore LV transformers are excluded from these regulations.

The most significant innovation of [14] is the introduction of optional accuracy classes for Wideband (WB). For the first time, standardized accuracy requirements for harmonic measurement are defined for all devices in this family. The defined classes are: WB0 (up to the 13th harmonic), WB1 (up to 3 kHz), WB2 (up to 20 kHz), WB3 (up to 150 kHz), and WB4 (up to 500 kHz). This innovation addresses the need to monitor high-frequency harmonic distortion caused by the penetration of power electronics-based devices (PV inverters, wind turbines, and High Voltage Direct Current (HVDC) converter stations). Traditional instrument transformers are neither designed nor tested to perform PQ measurements. Table 1.1 shows the accuracy index limits for the WB0 band, which was already regulated in the previous version of the standard. Conversely, table 1.2 shows the new accuracy limits proposed for the new WBs. WB0 and WB1 are the frequency ranges of the so-called, PQ band, which reaches up to 2.5 kHz for 50 Hz systems and 3 kHz for 60 Hz systems.

Table 1.1: WB0 extension for harmonics

	Ratio Error at harmonics [%]			
Accuracy Class	**2nd to 4th**	**5th and 6th**	**7th to 9th**	**10th to 13th**
0.5	±5	±10	±20	±20
1	±10	±20	±20	±20
	Phase displacement at harmonics [mrad]			
0.5	±87	±174	±349	±349
1	±174	±349	±349	±349

Table 1.2: Accuracy class extensions for wide bandwidth applications

	Ratio error at the frequencies shown below [%]		
Accuracy class	$f_r < f \leq 1\,\text{kHz}$	$1 < f \leq 1.5\,\text{kHz}$	$1.5 < f \leq 3\,\text{kHz}$
WB1	$f_r < f \leq 1\,\text{kHz}$	$1 < f \leq 1.5\,\text{kHz}$	$1.5 < f \leq 3\,\text{kHz}$
WB2	$f_r < f \leq 5\,\text{kHz}$	$5 < f \leq 10\,\text{kHz}$	$10 < f \leq 20\,\text{kHz}$
WB3	$f_r < f \leq 20\,\text{kHz}$	$20 < f \leq 50\,\text{kHz}$	$50 < f \leq 150\,\text{kHz}$
WB4	$f_r < f \leq 50\,\text{kHz}$	$50 < f \leq 150\,\text{kHz}$	$150 < f \leq 500\,\text{kHz}$
0.5	±5	±10	±10
1	±10	±20	±30

	Phase error at the frequencies shown below [mrad]		
Accuracy class	$f_r < f \leq 1\,\text{kHz}$	$1 < f \leq 1.5\,\text{kHz}$	$1.5 < f \leq 3\,\text{kHz}$
WB1	$f_r < f \leq 1\,\text{kHz}$	$1 < f \leq 1.5\,\text{kHz}$	$1.5 < f \leq 3\,\text{kHz}$
WB2	$f_r < f \leq 5\,\text{kHz}$	$5 < f \leq 10\,\text{kHz}$	$10 < f \leq 20\,\text{kHz}$
WB3	$f_r < f \leq 20\,\text{kHz}$	$20 < f \leq 50\,\text{kHz}$	$50 < f \leq 150\,\text{kHz}$
WB4	$f_r < f \leq 50\,\text{kHz}$	$50 < f \leq 150\,\text{kHz}$	$150 < f \leq 500\,\text{kHz}$
0.5	±87	±174	±349
1	±174	±349	±349

Parts 2, 3, 4 and 5 define specific requirements for ITs based on traditional inductive technology, which still constitute a large portion of existing installed devices. Among these, as already seen, there are: (i) CTs and VTs, the combined ones –CTs plus VTs in the same enclosure. Finally section 5 focuses on HV applications by defining the requirements for CVTs. The latter use a capacitive voltage divider to reduce the high line voltage to an intermediate value, which is then further reduced by a inductive transformer.

Parts 7, 8, 10 and 11 define specific requirements for LPITs. These devices can be further divided into active and passive, with the RC being one of the passive types.

Parts 14 and 15 standardize measurement devices for DC applications, due to the growing popularity of HVDC transmission systems, essential for long-distance power transmission from large renewable energy plants and for interconnecting asynchronous grids.

Part 9 defines the digital interface for instrument transformers and in particular standardizes the methods of digitizing and transmitting measured values. It is part of the broader ecosystem of the IEC 61850 standard [17], the fundamental standard for substation automation.

Part 13 standardizes Stand-Alone Merging Units (SAMUs) which acts as a bridge between the analog and digital worlds for legacy inductive ITs since their analog outputs reach values that are not compatible with digital instruments, such as 1 A, 5 A, 100 V

In conclusion, this series of documents creates a comprehensive framework of requirements, including those related to construction, accuracy, operating temperature range, and EMC. It also provides detailed guidelines for manufacturing processes, testing procedures, quantities ratings, influence quantities, and insulation coordination. Being compliant with these standards is essential for ensuring the consistency and reliability of ITs operation in power system in order to achieve accurate measurements for protection and monitoring purposes. However, IEC 61869 does not specify a preferred methodology to perform an uncertainty evaluation. Therefore, standards leave operators some flexibility in choosing the most appropriate procedure among the various internationally established methods, such as [18] and [19] based on the context and available information.

For clarity, table 1.3 lists all documents discussed.

Table 1.3: Family of standards IEC 61869

Document	Title
IEC 61869-1:2023 [14]	General requirements
IEC 61869-2:2012 [20]	Additional requirements for CTs
IEC 61869-3:2011 [21]	Additional requirements for VTs
IEC 61869-4:2013 [22]	Additional requirements for combined transformers
IEC 61869-5:2011 [23]	Additional requirements for CVTs
IEC 61869-9:2016 [24]	Digital interface for ITs
IEC 61869-10:2017 [13]	Additional requirements for LPCTs
IEC 61869-11:2017 [25]	Additional requirements for LPVTs
IEC 61869-13:2021 [26]	Stand-Alone Merging Units (SAMUs)
IEC 61869-14:2018 [27]	Additional requirements for CTs for DC applications
IEC 61869-15:2018 [28]	Additional requirements for VTs for DC applications
IEC 61869-20:2025 [29]	Safety requirements for HV ITs
IEC 61869-99:2022 [11]	Glossary
IEC TR 61869-100:2017 [30]	Guidance for application of CTs in protection
IEC TR 61869-102:2014 [31]	Ferroresonance with inductive VTs in substations
IEC TR 61869-103:2012 [32]	Use of ITs for PQ measurement

Chapter 2

Evaluation of Measurement Uncertainty

Measurements and their associated operations are undeniably interdisciplinary in nature and play a prominent, constantly growing role in a variety of sectors, from the technical and industrial to the commercial and legal. Therefore, determining the uncertainty – which will inevitably affect all measurement results – and defining internationally shared procedures to evaluate the uncertainty have become a crucial and critical tasks. For metrologists around the world, the *Guide to the Expression of Uncertainty in Measurement (GUM)* [18] is the document to refer to as it provides the basic tools and general rules to evaluate and indicate the uncertainty to be associated with the result of a measurement.

This chapter reviews the core concepts and foundational definitions of metrology presented in the GUM [18], and details the standard procedures for the evaluation of measurement uncertainty, which are based on the Law of Propagation of Uncertainty (LPU). It then delves deeper into Supplement 1 [19] which describes the implementation procedure of the Monte Carlo method (MCM). These tools will be essential for understanding the metrological aspects discussed in the following sections.

2.1 "GUM" Guide

2.1.1 Introduction to the Measurement

To standardize the evaluation of measurement uncertainty worldwide, the standard GUM [18] was published by the Joint Committee for Guides in Metrology (JCGM). This organization includes members from the following international bodies working in the field of metrology: (i) International Bureau of Weights and Measures (BIPM), (ii) IEC, (iii) International Federation of Clinical Chemistry and Laboratory Medicine (IFCC), (iv) International Laboratory Accreditation Cooperation (ILAC), (v) International Organization for Standardization (ISO), (vi) International Union of Pure and Applied Chemistry (IUPAC), (vii) International Union of Pure and Applied Physics (IUPAP) and (viii) International Organization of Legal Metrology (OIML).

Understanding the concepts of (i) *quantity*, (ii) *measurement process*, (iii) *measurand*, (iv) *measurement uncertainty*, (v) *measurement accuracy*, and (vi) *influence quantity* is essential before performing any measurement. For this purpose, the JCGM publishes a foundational guide to metrological definitions: *International Vocabulary of Metrology (VIM)* [12]. In this document, the following technical definitions are adopted:

- *quantity*: "property of a phenomenon, body, or substance, where the property has a magnitude that can be expressed as a number and a reference" (i.e. the unit of measurement) [12].
- *measurement*: "process of experimentally obtaining one or more quantity values that can reasonably be attributed to a quantity" [12].
- *measurand*: "quantity intended to be measured" [12].
- *measurement uncertainty*: "non-negative parameter characterizing the dispersion of the quantity values being attributed to a measurand, based on the information used" [12].
- *measurement accuracy*: "closeness of agreement between a measured quantity value and a true quantity value of a measurand. A measurement is said to be more accurate when it offers a smaller measurement error" [12].

- *influence quantity*: "quantity that, in a direct measurement, does not affect the quantity that is actually measured, but affects the relation between the indication and the measurement result" [12].

Operationally, the *purpose of a measurement* is to *experimentally* determine the value of a specific *property of the measurand*. However, any measurement result is always an *estimate* of the measurand's value, and it must be associated with a measurement *uncertainty*. Such uncertainty defines a *range* within which the "true value" of the measurand is believed to lie with a *stated probability*, although it is possible for the actual value to be outside this range. Finally, uncertainty can also be seen as the result of *incomplete knowledge* of the measurand, arising from various *influence quantities* –acting as *sources of error* that influence the result of a measurement–, such as: (i) the physical model of the measurand, (ii) the environmental conditions, (iii) the response of the instrumentation used in the measurement system, and (iv) simplifications in the measurement process. Once the uncertainties have been calculated, the results obtained from different measurements (using different instruments and methods) can be compared to determine the most *accurate* and reliable one.

For completeness, the following table 2.2 lists all current publications of the JCGM's metrology guides.

2.1.2 Calculation of Uncertainty according to the "GUM"

The GUM [18] provides guidelines for evaluating and expressing measurement uncertainty.

In most cases, the measurand Y is a function f of N input measured quantities $X_1, X_2, \ldots, X_N$.

$$Y = f(X_1, X_2, \ldots, X_N) \tag{2.1}$$

First, it must be noted that the input quantities $X_1, X_2, \ldots, X_N$ are themselves estimated $x_1, x_2, \ldots, x_N$ and consequently have their own associated uncertainties $u(x_1), u(x_2), \ldots, u(x_N)$. Therefore, equation (2.1) can be rewritten as:

$$y = f(x_1, x_2, \ldots, x_N) \tag{2.2}$$

Table 2.1: JCGM Publications

Document	Short title	Main content	When to use it
JCGM 100:2008 [18]	GUM (base guide)	Evaluation of measurement uncertainty via LPU.	Standard cases.
JCGM 101:2008 [19]	Supplement 1 (MCM)	Propagation of distributions via MCM	When LPU is inadequate.
JCGM 102:2011 [33]	Supplement 2 (multiple outputs)	Multiple output quantities. MCM.	When several measurands are reported together.
JCGM 106:2012 [34]	Uncertainty in conformity decisions	Use of uncertainty in conformity assessment: decision rules, tolerance limits, guard bands, risk management.	To set acceptance and rejection criteria.
JCGM GUM-6:2020 [35]	Part 6 — Measurement models	Developing and using measurement models: defining the measurand, influence quantities; choosing between LPU and MCM.	When the measurement model must be built and justified before evaluating uncertainty.
JCGM GUM-1:2023 [36]	Part 1 — Introduction	Overview of the modern GUM suite; high-level guidance on method selection.	As an orientation guide and to cite the overall framework.
JCGM 200:2012 [12]	VIM	International vocabulary of metrology: core concepts and terms.	To ensure consistent terminology.

In this way, there is the switch from physical quantities Y and $X_1, X_2, \ldots, X_N$ to their corresponding estimates y and $x_1, x_2, \ldots, x_N$. In conclusion, to calculate $\boldsymbol{y}$–the best estimate of the measurand $\boldsymbol{Y}$)–and the associated combined standard uncertainty $u_c(y)$–the dispersion of the measurand Y–, it is necessary to calculate the best estimates $x_1, x_2, \ldots, x_N$ of input quantities and their standard uncertainty $u(x_1), u(x_2), \ldots, u(x_N)$ first. For this purpose, the GUM proposes two methods for assessing uncertainty: *type A* and *type B*.

To evaluate ***type A*** uncertainty, statistical methods must be used on the series of measured values –observations or samples– of the same measurand. For instance, if M measured values are available, the best estimate x_k of X_k is the arithmetic mean of the M values and the best estimate of the standard uncertainty $u(x_k)$ is the sample standard deviation, which can be calculated as follows:

$$x_k = \frac{1}{M} \sum_{n=1}^{M} x_{k,n} \tag{2.3}$$

$$u(x_k) = \sqrt{\frac{1}{(M-1)} \sum_{n=1}^{M} \left(x_{k,n} - x_k\right)^2} \tag{2.4}$$

Furthermore, in cases where the central limit theorem holds, the standard uncertainty of the mean becomes:

$$u(x_k) \simeq \frac{u(x_k)}{\sqrt{M}} = \sqrt{\frac{1}{M(M-1)} \sum_{n=1}^{M} (x_{k,n} - x_k)^2} \tag{2.5}$$

Therefore, as the number of M repetitions increases, the standard uncertainty decreases.

To evaluate ***type B*** uncertainty, non-statistical methods must be used; specifically, it is necessary to take into account all the available information: (i) knowledge of the human operator, (ii) the experience gained from similar tests carried out in the past, (iii) certificates of calibration, and (iv) the data-sheets of the instrumentation used.

Once $x_1, x_2, \ldots, x_N$ and $u(x_1), u(x_2), \ldots, u(x_N)$ are obtained, the ***combined standard uncertainty*** can be calculated as follows:

$$u_c(y) = \sqrt{\sum_{i=1}^{N} \left(\frac{\partial f}{\partial x_i}\right)^2 u^2(x_i)} \tag{2.6}$$

Equation (2.6) is known as LPU and is valid only for *uncorrelated* quantities X_i. However, if the quantities are *correlated*, equation (2.6) must be expressed as follows:

$$u_c(y) = \sqrt{\sum_{i=1}^{N} \left(\frac{\partial f}{\partial x_i}\right)^2 u^2(x_i) + 2\sum_{i=1}^{N-1}\sum_{j=i+1}^{N} \frac{\partial f}{\partial x_i}\frac{\partial f}{\partial x_j} u(x_i, x_j)} \tag{2.7}$$

where the partial derivatives $\frac{\partial f}{\partial x_i}$ are called *sensitivity coefficients* and $u(x_i, x_j)$ is the *covariance* between x_i and x_j. Then, the *correlation coefficient* can be defined as:

$$\rho(x_i, x_j) = \frac{u(x_i, x_j)}{u(x_i)\, u(x_j)} \tag{2.8}$$

$\rho(x_i, x_j)$ can take a value between -1 and 1. In particular, when $\rho(x_i, x_j)$ is equal to 0, the quantities x_i and x_j are uncorrelated.

Finally, substituting the covariance of equation (2.8) in equation (2.7), the following mathematical expression is obtained:

$$u_c(y) = \sqrt{\sum_{i=1}^{N} \left(\frac{\partial f}{\partial x_i}\right)^2 u^2(x_i) + 2\sum_{i=1}^{N-1}\sum_{j=i+1}^{N} \frac{\partial f}{\partial x_i}\frac{\partial f}{\partial x_j} \rho(x_i, x_j)\, u(x_i)\, u(x_j)} \tag{2.9}$$

To obtain equation (2.6), the first-order Taylor series approximation of the measurement function f of equation (2.2) is performed. Therefore equation (2.6), equation (2.7) and equation (2.9) are valid if f is linear. However, in many real cases, even if it is not linear, the LPU can be considered valid in evaluating the measurement uncertainty since the uncertainty is much lower than the value of the measurand. In cases where the function f is highly nonlinear, it is necessary to increase the order of the Taylor expansion terms or use other methods to assess uncertainty, for example, the MCM method described in Supplement 1 of the GUM [19].

2.2 Supplement 1 to the "GUM"

Evaluating the uncertainty of an indirect measurement via the LPU, contained in [18], can become challenging to apply –for instance, when the measurement model is hard to formalize or when the input Probability Density Functions (PDFs) do not have a Gaussian profile. In such situations, [19] suggests MCM, which propagates the known PDFs of the input quantities to determine the PDF for the output quantity. If such a PDF is known, it is possible to calculate: (i) an estimate of the output quantity, (ii) the standard uncertainty associated with this estimate, and (iii) a coverage interval for that quantity, corresponding to a specified coverage probability.

To implement a MCM, the practical steps to follow are:

- choose the M repetitions to perform the MCM,
- define the output quantity Y and the input quantities X_i,
- develop a model $Y = f(X_i)$ which relates Y to X_i,
- assign the PDF to the X_i based on available information. For instance, a typical PDF selection for the input variables might consist of choosing a rectangular distribution when there is no information available,
- propagate the PDFs of the input variables X_i to obtain the PDF of Y by means of the developed model. This is done by: (i) generating M samples, (ii) calculating M values of Y by means of the model f, (iii) sorting the obtained Y values in ascending order, and finally (iv) calculating average value, standard deviation and coverage interval of Y through the estimated PDF.

Chapter 3

Modelling and Characterization of Low-power Current Transformers

3.1 Simplifying Rogowski Coil Modeling: Simulation and Experimental Verification

The widespread use of RC in numerous applications justifies the interest in the development of RC models. Although several models are available in the literature, their practical implementation is often complex and non-immediate. For instance, the high-frequency behavior of the RC is investigated in [37] using the classical lumped model, while [38] examines another high-frequency modeling approach based on a black-box conceptualization of the Rogowski derived from preliminary measurements on the device. [39] presents a highly detailed model which relies on equations that require the complete geometry of the device and the space in which it is installed. An electro-thermal model written in VHDL-AMS language and based on finite element analysis (FEA) is described in [40]. A RC is designed from scratch for three-phase current measurement in electric motors in [41]. Finally, the same authors in [42] conceptualized a simple model, although based on several preliminary measurements. All these studies propose sophisticated models and custom-designed applications for RCs. Therefore, to address this gap, the primary goal of this work is to propose a novel and straightforward modeling procedure for determining the input-output relationship –i.e. a frequency model– of any given commercial RC.

From a measurement point of view, the proposed methodology relies solely on the external geometric parameters of the RC, thus eliminating the need for preliminary and additional electrical measurements. However, any available electrical data can be used to further refine and validate the model. Therefore, the method's primary strength lies in its use of data readily available from the datasheet of the transducers under analysis. In conclusion, it is a simplified procedure.

This simplification offers several significant advantages, including: (i) the a priori estimation of the RC frequency response, eliminating the need for extensive and equipment-intensive laboratory characterization, and (ii) the proposal of an additional RC model that can be integrated into simulations to reproduce an actual current measurement, being the use of real-time power network simulators increasingly common.

Section 3.1 is structured as follows: (i) model conceptualization, (ii) model validation, and (iii) discussion of results and conclusions.

3.1.1 Modelling Procedure

The proposed modelling procedure is outlined in figure 3.1.

As a ***first step***, the procedure starts from the knowledge of the RC geometric parameters which can be obtained through operator direct measurement or from the sensor datasheet. Looking at figure 1.6, the first step requires the measurement of the internal diameter $2a$ and the diameter of the support section d. The proposed frequency modeling procedure takes into consideration three distinct cross-sectional geometries: (i) circular, (ii) square or rectangular, and (iii) oval. The latter two configurations necessitate an extra measurement, as detailed in figure 3.2.

As a ***second step***, the procedure involves selecting specific parameters from the device datasheet. The two parameters essential for the model are the (i) winding resistance and (ii) the Transformation Ratio (TR). Other typical parameters provided in RC datasheets are listed in table 3.2. The model's Transfer Function (TF) also includes the value of the rated burden. If this is not specified by the manufacturer, a standard value of $2\,\mathrm{M}\Omega$ is assumed, as recommended in [14].

The ***third step*** of the procedure determines the value of the mutual inductance M. This is achieved by moving in the frequency domain. Therefore, assuming a system in sinusoidal regime with pulsation $\omega = 2\pi f$, the Fourier transform can be applied to the equation (1.7) and consequently the time derivative operator $\frac{d}{dt}$

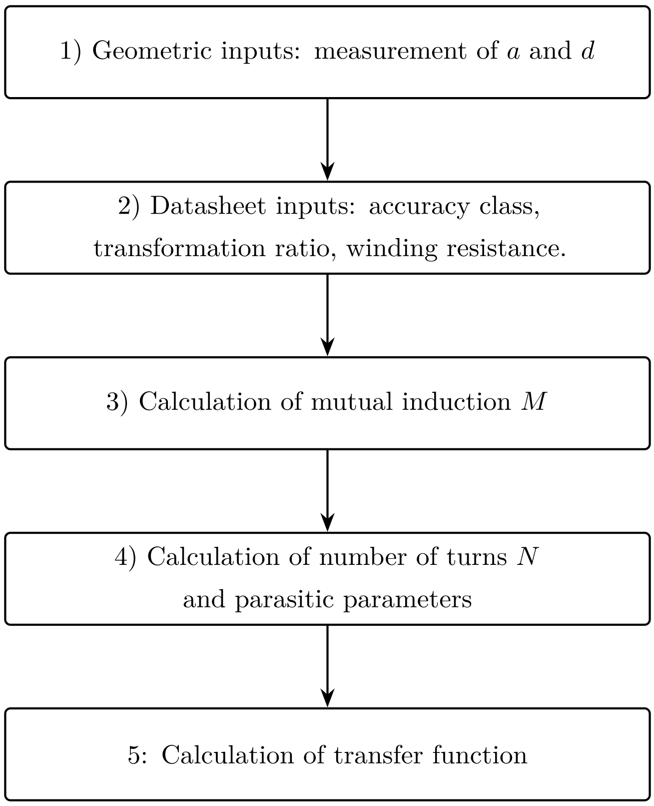

Figure 3.1: Flowchart of the modelling procedure.

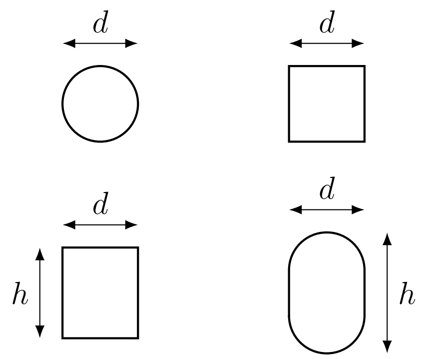

Figure 3.2: Possible cross-sections for the Rogowski coil support.

becomes a multiplication by $j\omega$, obtaining:

$$\vec{U_s} = M(j\omega)\vec{I_p}, \tag{3.1}$$

where $\omega = 2\pi f$ is the angular frequency of the measured primary current with frequency f. Afterwards, using the rated TR at 50 Hz (TR_{50}), M is calculated as:

Table 3.1: Typical parameters available in the RC datasheet.

Accuracy Class	Linearity Error	Winding Resistance	Transformation Ratio
Max Current	Bandwidth	Temperature Class	Rated Burden

$$M = \frac{TR_{50}}{2\pi 50}. \tag{3.2}$$

The ***fourth step*** addresses the physical geometry of the RC. Based on the dimensions determined in the first step, the perimeter and cross-sectional area of the RC under test are calculated. Subsequently, the number of turns N of the RC is determined by inverting established formula for mutual inductance, as presented in [43, 44, 45]. This step is significant because, from a practical point of view, the number of turn N is a parameter that is often omitted from transducer datasheet, posing a critical challenge to accurate modeling. Rearranging the mutual inductance formulas for each type of cross-section, the following equations are obtained:

$$N_{rec} = \frac{2\pi M}{d\,\mu\,\log\left(\frac{2a+2d}{2a}\right)}, \tag{3.3}$$

$$N_{cir} = \frac{2M}{\mu\left(2a + d - 2\sqrt{(a+b)a}\right)}, \tag{3.4}$$

$$N_{ova} = \frac{2\pi M}{\mu\left(2a + d - 2\sqrt{(a+b)a} + \frac{h}{\pi}\,\log\left(\frac{a+b}{a}\right)\right)}, \tag{3.5}$$

where μ is the overall permeability, and N_{rec}, N_{cir}, and N_{ova} are the number of turns of the rectangular, circular, and oval cross-section, respectively. Subsequently, thanks to knowledge of the winding geometry, it is possible to calculate the length l_w, cross-section A_w, and radius r_w of the single coil of wire wrapped around the support, which will then be used in the next step of the procedure.

The ***last step*** is the calculation of the parasitic parameters of the RC:

$$C_i = \frac{2\,\varepsilon\,\pi^2\,(2a+d)}{\log\left(\frac{\sqrt{A_i/\pi}}{r_w}\right)}, \tag{3.6}$$

$$L_{rec} = \frac{\mu\, d\, \log\left(\frac{a+d}{a}\right)\, N_{\mathrm{rec}}^2}{2\pi}, \tag{3.7}$$

$$L_{cir} = \frac{\mu\, N_{\mathrm{cir}}^2 \left(2a + d - 2\sqrt{(a+d)a}\right)}{2}, \tag{3.8}$$

$$L_{ova} = \frac{\mu\, N_{\mathrm{ova}}^2 \left(2a + d - 2\sqrt{(a+d)a} + \frac{h}{\pi}\log\left(\frac{a+d}{a}\right)\right)}{2\pi}. \tag{3.9}$$

where ε represents the vacuum permittivity, while C and L denote the parasitic capacitance and inductance, respectively. The subscript i is used to index the different cross-sectional parameters (e.g., A_i). A brief discussion of permeability and permittivity is needed. A general notation has been preferred so that relative permeability or permittivity can be introduced if the specific RC configuration requires it. Otherwise, using only vacuum permeability and permittivity is correct.

Finally, the simplified electrical model of a RC is shown in figure 3.3. It consists of: a voltage source –representing the induced voltage by the primary current– in series with the resistance R_w and the parasitic inductance of the coil L and in parallel with the parasitic capacitance between the winding and the return coil C and the input impedance of the acquisition system Z connected in cascade to the RC.

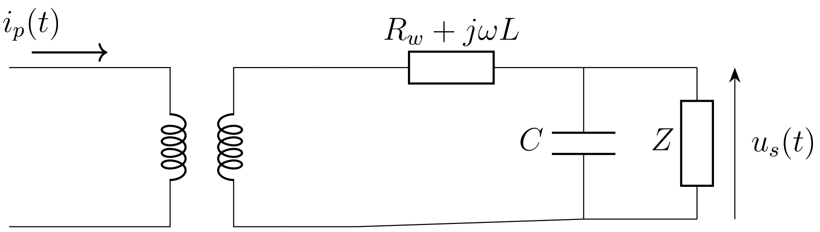

Figure 3.3: Schematic of the equivalent circuit of the Rogowski coil

From circuit analysis of figure 3.3, the TF of RC in the "s" domain is derived defining the input-output relation between the measured voltage and the primary current:

$$TF(s) = \frac{Z\, M\, s}{Z\, C\, L\, s^2 + s(L + R_w\, C\, Z) + R_w + Z}, \tag{3.10}$$

all the parameters in equation (3.10) were previously described. The winding resistance R_w can be determined by direct measurement or from the manufacturer's specifications. Chapter B describes the proof of the transfer function of equation (3.10).

3.1.2 Model Validation

3.1.2.1 Validation by Simulation

The performance of the proposed procedure is verified through two distinct simulations. First, a *frequency sweep* test is conducted to evaluate the model's accuracy as a function of frequency. Second, a *MCM analysis* is employed to quantify the impact of uncertainty sources on the model's overall accuracy. All simulations are performed in the MATLAB environment.

For the frequency sweep, a sinusoidal current with an amplitude of 1000 A and a 0° initial phase is initially generated. Subsequently, the frequency of each waveform ranges from 50 Hz to 2500 Hz in 50 Hz increments to cover the standard PQ analysis range, while the amplitude of each harmonic is defined by the values in Table 5 contained in the standard [46]. The designed signals are simulated over a 200 ms time window with a sampling rate of 50 kSa/s. Finally, the RC response is obtained by multiplying the RC TF –equation (3.10)– by each simulated input signal. The parameters of the RC TF will be discussed in detail later.

The accuracy of the RC response is evaluated via the Fast Fourier Transform (FFT) by calculating two standard performance metrics –the ratio error $\varepsilon(\%)$ and phase displacement $\Delta\phi$–:

$$\varepsilon(\%) = \frac{TR_f I_{sf} - I_{pf}}{I_{pf}} \times 100 \tag{3.11}$$

$$\Delta\phi = \hat{I}_{sf} - \hat{I}_{pf}, \tag{3.12}$$

where TR_f is the TR; I_{sf} and I_{pf} are the Root Mean Square (RMS) values of the secondary and primary currents, respectively, evaluated at the generic frequency f. Analogously, $\hat{I}_{sf}$ and $\hat{I}_{pf}$ are the phase angles of the secondary and primary currents, respectively.

The results of the initial tests are summarized graphically in figure 3.4 and presented in table 3.3. For this example test, the simulated device is a RC with a rectangular cross-section and a 0.5 accuracy class. The obtained outcomes demonstrate that the estimation of the RC output is highly accurate across all tested PQ frequency ranges. Furthermore, the magnitude of the calculated error indices falls within the range of possible admissible values for the nominal accuracy class of the simulated device. The permissible limits for the ratio error and phase displacement for each harmonic up to the 13th are specified in [14].

Table 3.3: $\varepsilon(\%)$ and $\Delta\varphi$ for each test signal applied to a rectangular RC.

Frequency (Hz)	ε (%)	$\Delta\varphi$ (mrad)	**Frequency (Hz)**	ε (%)	$\Delta\varphi$ (mrad)
50	−0.01	3.2	1300	−0.12	81.9
100	−0.01	6.3	1350	−0.13	85.1
150	−0.01	9.5	1400	−0.14	88.2
200	−0.01	12.6	1450	−0.15	91.4
250	−0.01	15.8	1500	−0.16	94.5
300	−0.02	18.9	1550	−0.17	97.7
350	−0.02	22.1	1600	−0.18	100.9
400	−0.02	25.2	1650	−0.19	104.0
450	−0.02	28.4	1700	−0.20	107.2
500	−0.03	31.5	1750	−0.21	110.3
550	−0.03	34.7	1800	−0.23	113.5
600	−0.03	37.8	1850	−0.24	116.6
650	−0.04	41.0	1900	−0.25	119.8
700	−0.04	44.1	1950	−0.26	122.9
750	−0.05	47.3	2000	−0.28	126.1
800	−0.05	50.4	2050	−0.29	129.2
850	−0.06	53.6	2100	−0.30	132.4
900	−0.06	56.7	2150	−0.32	135.5
950	−0.07	59.9	2200	−0.33	138.7
1000	−0.08	63.0	2250	−0.35	141.8
1050	−0.08	66.2	2300	−0.36	145.0
1100	−0.09	69.3	2350	−0.38	148.1
1150	−0.10	72.5	2400	−0.39	151.3
1200	−0.11	75.6	2450	−0.41	154.4
1250	−0.11	78.8	2500	−0.43	157.6

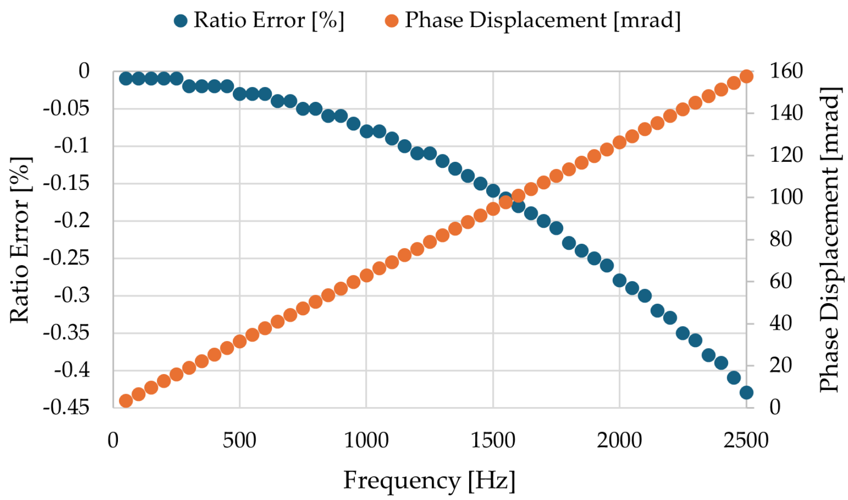

Figure 3.4: $\varepsilon(\%)$ and $\Delta\phi$ for each test signal applied to a rectangular RC.

A key aspect of validating a new method is to identify and assess the main sources of uncertainty. Therefore, for the proposed modeling approach, the main sources of uncertainty identified are the geometric measurements of the transducer under analysis, which are assumed during this first simulation phase, while they will be physically performed later. In fact, although numerous influence quantities affect RC performance during normal working operation, this analysis is specifically focused on the uncertainty sources that directly impact the proposed procedure. In conclusion, the dimensions: (i) d, (ii) h (figure 3.2), and (iii) a (figure 1.6) are treated as the input quantities of the MCM analysis. Additionally, the winding resistance, R_w, is included and its value may be reported in the RC datasheet or measured directly. For these input parameters, a uniform PDF centered on the parameter value is chosen. These distributions have a width equal to twice the 1 %, 10 % and 20 % of the value of the chosen parameter. For the sake of brevity, the MCM results presented in table 3.4 refer to the case of a RC having rectangular cross-section of side 8 mm, an internal "diameter" of 100 mm and a winding resistance of 210 ohms –the same considered in table 3.3 and figure 3.4.

Table 3.4: Results of the uncertainty analysis for a rectangular RC.

Uncertainty Considered (%)	**Quantity**	$\boldsymbol{\mu}$	$\boldsymbol{l_{95\%}}$	$\boldsymbol{u_{95\%}}$
1	N (–)	1340	1309	1370
10	N (–)	1350	1054	1665
20	N (–)	1402	837	2092
1	C (F)	3.8×10^{-12}	3.8×10^{-12}	3.9×10^{-12}
10	C (F)	3.9×10^{-12}	3.4×10^{-12}	4.3×10^{-12}
20	C (F)	3.9×10^{-12}	3.0×10^{-12}	4.6×10^{-12}
1	L (H)	4.3×10^{-4}	4.2×10^{-4}	4.4×10^{-4}
10	L (H)	4.3×10^{-4}	3.3×10^{-4}	5.3×10^{-4}
20	L (H)	4.5×10^{-4}	2.7×10^{-4}	6.6×10^{-4}

The outputs of the MCM analysis are presented for each quantity affected by uncertainty and uncertainty level, providing the mean value μ and the 95% confidence interval, consisting of the lower limit $l_{95\%}$ and upper limit $u_{95\%}$. The number of trials of the MCM is equal to 10000. As expected, a greater input uncertainty of the sources of uncertainty leads to a wider spread in the calculated results. Despite this, the RC model's parasitic parameters show low sensitivity to the sources of uncertainty chosen as input of the MCM. On the contrary, the parameter most significantly affected is the number of turns; notably, this is a quantity that the proposed method already estimates with high accuracy.

3.1.2.2 Validation by Measurements

To evaluate the practical usefulness and applicability of the proposed approach, an experimental validation is performed using three commercial RCs, designated RC1, RC2, and RC3. Table 3.5 lists the specification of such RCs.

Table 3.5: Datasheet comparison for the three commercial RCs.

Feature	**RC1**	**RC2**	**RC3**
TR50 ($\mathrm{mV\,kA^{-1}}$)	100	100	100
d (mm)	8	8	12
a (mm)	50	57	21.5
R_{w} (Ω)	256	381	22
Cross-Section	Circular	Circular	Circular
Technology	Split core	Split core	Split core
Accuracy Class	0.5	1	1
Bandwidth	1 Hz–100 kHz	N.A.	20 Hz–5 kHz
Operating Temperature	−30 °C to 80 °C	−20 °C to 85 °C	−20 °C to 70 °C
Rated Current (A)	1000	1000	1000

The tests are conducted using the measurement setup depicted in figure 3.5 and for clarity a color-coding scheme is used to distinguish between current and voltage signal paths. The system consists of a Fluke calibrator 6105A and a Fluke transconductance 52120A (with 120 A full scale) both in metrological confirmation, which are used in combination to generate the desired input current. This current is injected through the RCs under test and applied to the reference shunt of 1 $m\Omega$ which was previously characterized. By means of an accurate characterization procedure described in section 3.3.4.1, the shunt resistance was determined to be equal to 1.02129 $m\Omega \pm 0.00008$ $m\Omega$ for frequencies up to 2500 Hz. Finally, a National Instruments (NI) 9238 DAQ board, whose main specifications are given in table 3.7, is employed to collect the three voltage output signals from the RCs and the reference signal from the shunt using a LabVIEW program.

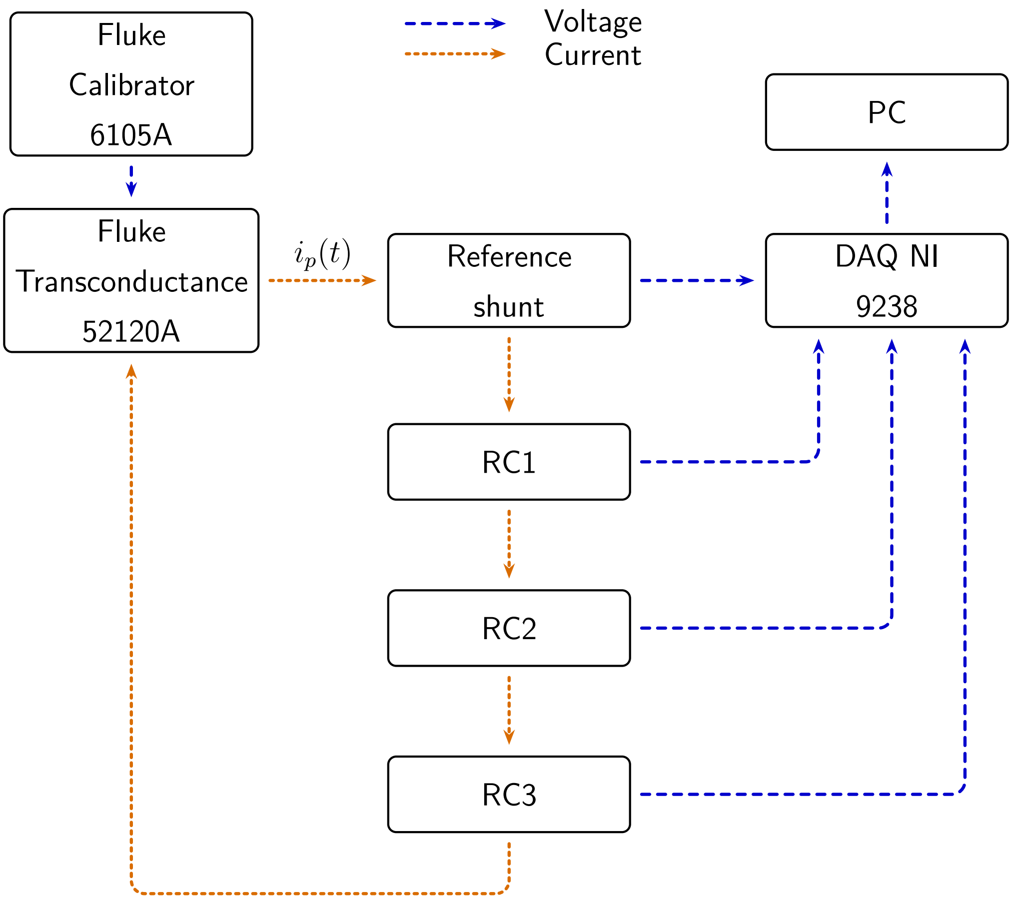

Figure 3.5: The measurement setup used for the experimental measurements on the commercial Rogowski coils.

Table 3.7: Main characteristics of the DAQ board NI 9238.

Bits	24-bit	**Voltage Range**	±500 mV
Sampling Frequency	50 kSa/s/Ch	**Input Impedance**	> 1 GΩ
Simultaneous Channels	Yes	**Gain Error**	±0.07%
Number of Channels	4	**ADC Type**	Delta Sigma
Offset Error	±0.005%	**Input Noise**	3.9 μV

The experimental validation involves injecting a sinusoidal primary current, generated by the Fluke generation system, through a reference shunt and the RCs under test. The test current is: (i) 100 A at 50 Hz, (ii) 50 A up to 850 Hz, and (iii) 36 A up to 2500 Hz. The estimated RC response is then computed by applying the model's TFs –from the proposed modeling procedure– to the acquired input signal –collected from the reference shunt. The result is an estimation of the RC behavior at each frequency. To validate and quantify the accuracy of this estimation, two performance indicators are used: (i) the Phase Error (PE), defined as the difference in milliradians between the phase displacement obtained from the simulated model and that from the experimental measurement, and the Voltage Difference (VD), defined as the percentage difference between the measured RC output voltage and the voltage estimated by the model, using the rated current as the basis for the ratio. For the sake of brevity, the results are listed in table 3.8 for a comprehensive selection of frequencies.

Table 3.8: Results from the comparison of actual and estimated RC behaviors.

	RC1		**RC2**		**RC3**	
Frequency (Hz)	**PE (mrad)**	**VD (%)**	**PE (mrad)**	**VD (%)**	**PE (mrad)**	**VD (%)**
50	2.92	0.4	−2.80	0.5	−4.41	1.8
250	14.36	1.2	−12.83	1.0	−15.88	4.2
550	31.39	2.7	−26.91	1.5	−33.66	8.9
850	48.34	4.6	−40.71	1.7	−51.73	13.5
1250	70.93	5.3	−59.10	0.8	−75.91	13.7
2500	141.77	15.8	116.92	−5.1	−151.31	22.8

3.1.3 Discussion of Results

The results demonstrate that the model provides an accurate estimation of the RC's behavior. As expected, a decrease in accuracy is observed at higher frequencies, which can be attributed to greater uncertainty in the signal generation system. Nevertheless, for all RCs and for almost all of the frequencies tested, the obtained errors are well below the limits specified in [14], with the only exception being the VD at 2500 Hz. Considering the simplifications inherent in the modeling procedure, these results are highly promising. The value of these findings is enhanced when viewed in the context of the intended final application; for example, systems with low target uncertainty will benefit significantly from the proposed method.

In conclusion, the results presented in this work provide a basis for discussion of the proposed method's strengths and limitations. First, the Matlab simulations and then the experimental measurements yielded encouraging outcomes, especially considering that this frequency model was intentionally developed to rely solely on few input parameters typically available in a manufacturer's datasheet, without requiring additional empirical measurements. This approach makes the methodology highly accessible since the operator does not need to be aware of any information about the internal structure of the device under test. A direct consequence of this datasheet-driven approach is that the model's accuracy could be significantly enhanced by incorporating supplemental empirical information such as one or more direct and accurate measurements of the RC's characteristics. For instance, characterizing the RC's response as a function of temperature could integrate the thermal dependence into the RC's TF, allowing the output to be estimated based on variations in operating temperature. This principle can be extended to include other influence quantities that affect RC performance. Consequently, the proposed modeling approach has several potential applications, including research laboratories, power system simulator development, and National Metrology Institutes (NMIs).

3.2 Individual or Group Error Compensation: An Experimental Demonstration on the Frequency Response of Rogowski Coils

ITs are key elements of modern power-systems. However, they are subjected to inherent errors due to manufacturing tolerances, environmental conditions, and operational stresses. Therefore error-compensation techniques —applied either at the individual device level or across groups— aim to mitigate these inaccuracies and consequently ensure compliance with standards. In particular, individual compensation calibrates each IT to its specific error profile, ensuring the maximum accuracy, but at greater cost and complexity. On the contrary, group compensation applies corrections based on averaged error characteristics across the batch of devices, offering cost savings but potentially sacrificing accuracy when device variability –within the same batch– is significant. The choice depends on the application: individual compensation is preferred for critical measurements, while group compensation may be enough for less sensitive tasks.

Specifically, this work studies the variability of three different batches of RCs subjected to varying temperatures, since the latter is recognized as an influence quantity for this type of devices.

Finally, it is important to note that the aim of this research is not to discuss or evaluate compensation techniques, but to emphasize the importance of clarity in deciding when to apply group versus individual error compensation.

Section 3.2 is structured as follows: (i) description of measurement setup and tests performed and (ii) discussion of results.

3.2.1 Description of the Measurement Setup and Tests

The tests are conducted using the measurement setup depicted in figure 3.6 and for clarity a color-coding scheme is used to distinguish between current and voltage signal paths.

The measurement setup consists of: (i) a Fluke 6105A calibrator driving a Fluke 52120A transconductance unit, both under metrological confirmation, (ii) a 1 $m\Omega$ reference shunt resistor whose characterization is described in section 3.3.4.1, (iii) a DAQ system comprising a chassis cDAQ-9174 with two NI-9238 modules—each providing 4 input channels, and (iv) a climatic chamber. The configuration also includes six nominally identical commercial RCs –same batch and manufacturer– placed together inside the climatic chamber. Table 3.10 summarizes the main characteristics of the three device types.

In brief, the calibrator controls the transconductance to generate a 50 Hz current $i_p(t)$ with amplitudes specified in table 3.9. This current flows through the six Rogowski Under Tests (RUTs) while the climatic chamber follows the temperature profile of figure 3.7. The outputs of the RUTs and the reference shunt are then acquired at three different times indicated figure 3.7 by a LabVIEW-controlled DAQ system.

The approach to tests consists of measuring the outputs of six nominally identical RUTs subjected to the same current and temperature conditions and more in general to the same influence quantities. Three RC types, called α, β, γ, from different manufacturers are selected; for each type, six identical sensors are tested. During setup design, the conductor carrying the test current is centered with respect to each RUT and all RUT are placed at equal distance from the conductor and among them, thereby minimizing external influences and isolating only the effects of temperature and current. The transconductance generates the primary test signals: 50 Hz sinusoidal currents with amplitudes increasing as specified in table 3.9. For each test signal, the DAQ system collects 100 single-tone frequency-response measurements from both the reference shunt and the six RUTs; each acquisition lasts 1 s.

As for the test temperatures, the selected setpoints are 20 °C, −5 °C and 40 °C in accordance with [14] and the temperature class of the RUTs. Although manufacturers are expected to provide the thermal time constant to determine the thermal steady-state condition, none of the tested devices included this information. Therefore, preliminary tests were carried out to estimate the RUTs' thermal time constant, at the end of which it was defined that 3 hours would guarantee thermal equilibrium without any doubt. Figure 3.7 shows the temperature cycle reproduced by the climatic chamber: (i) the ramp rate between any two setpoints is equal to $0.1\,°\mathrm{C\,min}^{-1}$, and (ii) the measurements are performed in three different time windows for each RUT type –one at each temperature setpoint– after waiting for the device to reach thermal equilibrium.

Table 3.9: Main features of the primary test signals

Frequency [Hz]	**Amplitude [A]**
	9
	25
50	50
	75
	90

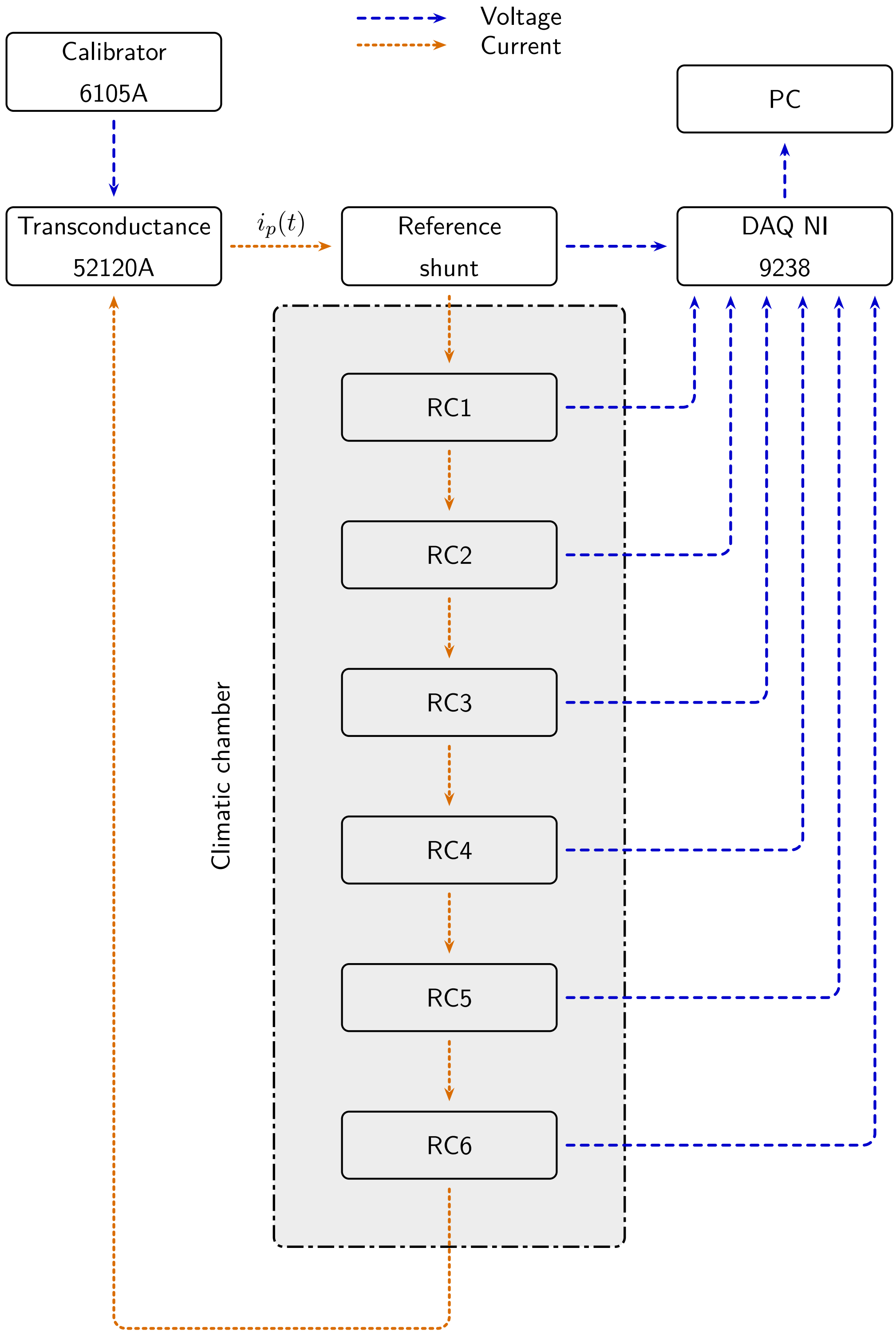

Figure 3.6: Block diagram of the measurement setup.

Table 3.10: Main features of the RUTs

	RUT α	**RUT** β	**RUT** γ
Accuracy	$\pm 0.5\,\%$	$\pm 1\,\%$	$\pm 1\,\%$
Ratio [mV/kA]	50	100	100
Rated current [kA]	0.1	1	1
Technology	Split-core	Split-core	Split-core

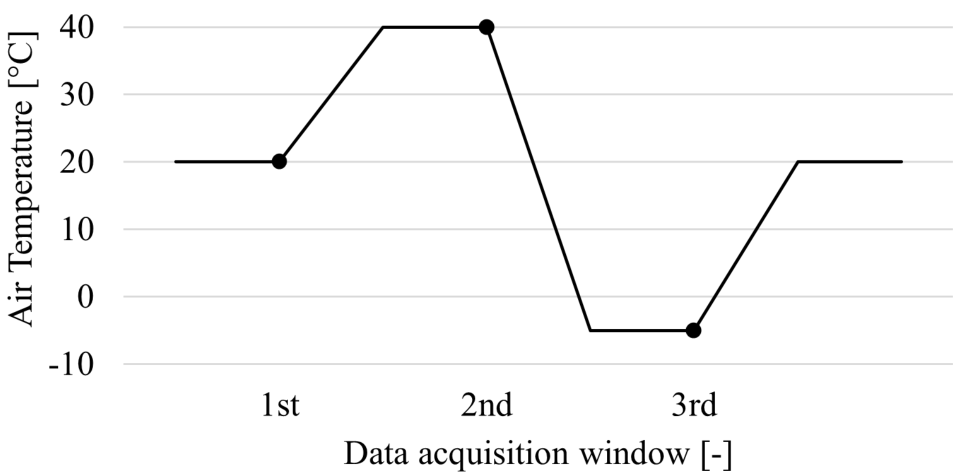

Figure 3.7: Temperature cycle accuracy test according to [14].

3.2.2 Discussion of the Results

To assess the experimental results, the ratio error $\varepsilon(\%)$ and phase displacement $\Delta\varphi$ are calculated according to the following formulas:

$$\varepsilon(\%) = \frac{K_r U_s - U_p}{U_p} \cdot 100, \tag{3.13}$$

$$\Delta\varphi = \varphi_s - \varphi_p, \tag{3.14}$$

where (i) K_r is the rated transformation ratio of the RUTs, (ii) U_p and U_s are the rms fundamental component of the primary and secondary, respectively, and (iii) φ_p and φ_s are the phase of the primary and secondary, respectively.

For the sake of clarity, the results are reported according to the following nomenclature. The letters α, β, and γ refer to a different manufacturer, as indicated in table 3.10. The numbers $1, 2, 3, 4, 5$, and 6, used in the tables reporting the results, refer to the six RCs of the same manufacturer tested together. For each RUT, all the obtained results are presented: (i) in table 3.11–table 3.13 for α-type RC, (ii) in table 3.14–table 3.16 for β-type RC, and (iii) in table 3.17–table 3.19 for γ-type RC.

Table 3.11: Ratio error and phase displacement for each α-type RUT at 20 °C

	Ratio Error [%] at 20 °C				
α-type RC	**9**	**25**	**50**	**75**	**90**
1	0.368	0.362	0.369	0.376	0.375
2	0.089	0.093	0.102	0.109	0.107
3	-0.086	-0.088	-0.081	-0.074	-0.076
4	0.289	0.289	0.296	0.303	0.301
5	-0.054	-0.056	-0.049	-0.042	-0.045
6	0.176	0.177	0.185	0.193	0.192
	Phase displacement [mrad] at 20 °C				
α-type RC	**9**	**25**	**50**	**75**	**90**
1	-0.46	-0.44	-0.45	-0.46	-0.46
2	-0.45	-0.47	-0.48	-0.48	-0.47
3	-0.46	-0.45	-0.46	-0.46	-0.45
4	-0.44	-0.46	-0.47	-0.47	-0.47
5	-0.45	-0.45	-0.46	-0.46	-0.46
6	-0.48	-0.48	-0.49	-0.50	-0.49

Beginning with a general observation, all tables (table 3.11–table 3.13) report results with significant digits that represent the associated standard deviation. For the α-type RCs, two observations stand out: (i) percentage variability in the ratio error values is greater than in the phase displacement values; and (ii) device-to-device variability among nominally identical sensors, at the same temperature and current, is greater than the variability observed for a given sensor as current increases. This behavior is consistent with the intrinsic linearity of RCs. Consequently, since the previous observations can be extended to other RUTs, the analysis of the remaining devices from other manufactures is restricted to the ratio error index and therefore phase displacement is no longer reported in following tables, as this research wants to investigate the most pronounced variability. A further note on table 3.11–table 3.13 is that, as expected, all devices satisfy the accuracy limits of their respective classes, but their accuracies are far from being similar in value. These experimental findings support the hypothesis that, even at 20 °C, group error compensation is neither suitable nor beneficial.

Table 3.12: Ratio error and phase displacement for each α-type RUT at 40 °C

	Ratio Error [%] at 40 °C				
α-type RC	**9**	**25**	**50**	**75**	**90**
1	0.114	0.111	0.119	0.107	0.098
2	-0.179	-0.178	-0.170	-0.182	-0.191
3	-0.366	-0.369	-0.362	-0.374	-0.383
4	0.039	0.036	0.044	0.032	0.022
5	-0.315	-0.320	-0.314	-0.326	-0.336
6	-0.090	-0.091	-0.083	-0.094	-0.102
	Phase displacement [mrad] at 40 °C				
α-type RC	**9**	**25**	**50**	**75**	**90**
1	-0.44	-0.42	-0.43	-0.44	-0.44
2	-0.48	-0.47	-0.47	-0.47	-0.47
3	-0.46	-0.44	-0.44	-0.45	-0.45
4	-0.46	-0.45	-0.45	-0.46	-0.46
5	-0.49	-0.45	-0.45	-0.45	-0.45
6	-0.49	-0.48	-0.48	-0.49	-0.49

Table 3.13: Ratio error and phase displacement for each α-type RUT at -5 °C

	Ratio Error [%] at -5 °C				
α-type RC	**9**	**25**	**50**	**75**	**90**
1	1.289	1.280	1.284	1.277	1.270
2	0.961	0.960	0.965	0.959	0.951
3	0.849	0.845	0.850	0.844	0.838
4	1.157	1.152	1.157	1.151	1.144
5	0.907	0.899	0.901	0.896	0.888
6	1.086	1.083	1.086	1.081	1.074
	Phase displacement [mrad] at -5 °C				
α-type RC	**9**	**25**	**50**	**75**	**90**
1	-0.41	-0.40	-0.40	-0.42	-0.42
2	-0.44	-0.44	-0.44	-0.45	-0.45
3	-0.41	-0.41	-0.42	-0.43	-0.43
4	-0.42	-0.43	-0.43	-0.44	-0.44
5	-0.42	-0.42	-0.43	-0.44	-0.43
6	-0.43	-0.45	-0.46	-0.47	-0.47

By looking at the following tables for β-type and γ-type (table 3.14–table 3.19), the observations already made above are reached: although both families exhibit good linearity over the tested current range and the six units within each family behave similarly, the variability of ratio error remains sufficient to undermine the effectiveness of group compensation.

Table 3.14: Ratio error for each β-type RUT at 20 °C

	Ratio Error [%] at 20 °C				
β-type RC	**9**	**25**	**50**	**75**	**90**
1	-0.314	-0.316	-0.305	-0.292	-0.313
2	-0.272	-0.274	-0.263	-0.250	-0.271
3	-0.371	-0.371	-0.359	-0.345	-0.366
4	-0.177	-0.177	-0.166	-0.152	-0.173
5	-0.221	-0.220	-0.205	-0.189	-0.210
6	-0.248	-0.244	-0.227	-0.210	-0.230

Table 3.15: Ratio error for each β-type RUT at 40 °C

	Ratio Error [%] at 40 °C				
β-type RC	**9**	**25**	**50**	**75**	**90**
1	-1.285	-1.284	-1.280	-1.274	-1.294
2	-1.241	-1.244	-1.239	-1.232	-1.254
3	-1.303	-1.305	-1.299	-1.291	-1.313
4	-1.140	-1.139	-1.135	-1.128	-1.149
5	-1.170	-1.171	-1.163	-1.153	-1.174
6	-1.211	-1.209	-1.199	-1.188	-1.208

Table 3.16: Ratio error for each β-type RUT at -5 °C

	Ratio Error [%] at -5 °C				
β-type RC	**9**	**25**	**50**	**75**	**90**
1	0.856	0.854	0.860	0.861	0.841
2	0.888	0.887	0.893	0.895	0.874
3	0.814	0.815	0.821	0.823	0.804
4	0.991	0.993	0.999	1.001	0.981
5	0.953	0.955	0.965	0.969	0.950
6	0.930	0.935	0.947	0.952	0.933

Table 3.17: Ratio error for each γ-type RUT at 20 °C

	Ratio Error [%] at 20 °C				
γ-type RC	**9**	**25**	**50**	**75**	**90**
1	-2.140	-2.150	-2.147	-2.146	-2.183
2	-2.102	-2.103	-2.098	-2.096	-2.132
3	-2.062	-2.070	-2.075	-2.079	-2.117
4	-2.109	-2.108	-2.091	-2.082	-2.116
5	-0.901	-0.911	-0.906	-0.906	-0.943
6	-1.981	-1.988	-1.979	-1.975	-2.011

Table 3.18: Ratio error for each γ-type RUT at 40 °C

	Ratio Error [%] at 40 °C				
γ-type RC	**9**	**25**	**50**	**75**	**90**
1	-1.916	-1.920	-1.907	-1.863	-1.802
2	-1.835	-1.836	-1.818	-1.772	-1.709
3	-1.803	-1.811	-1.800	-1.760	-1.701
4	-1.839	-1.834	-1.809	-1.757	-1.690
5	-0.637	-0.642	-0.627	-0.583	-0.520
6	-1.211	-1.209	-1.199	-1.188	-1.208

Table 3.19: Ratio error for each γ-type RUT at -5 °C

	Ratio Error [%] at -5 °C				
γ-type RC	**9**	**25**	**50**	**75**	**90**
1	-1.639	-1.638	-1.637	-1.624	-1.600
2	-1.602	-1.593	-1.595	-1.573	-1.548
3	-1.577	-1.582	-1.589	-1.576	-1.555
4	-1.642	-1.638	-1.615	-1.601	-1.572
5	-0.376	-0.380	-0.372	-0.363	-0.338
6	-1.474	-1.476	-1.460	-1.451	-1.425

Table 3.11 shows an interesting behaviour regarding the ratio error values of the α-type RUTs (and it is also representative of all types). For a measured current of 90 A, the six devices exhibit markedly different results, with variations ranging from about 50 % up to 600 % at 20 °C. This spread clearly illustrates the potential ineffectiveness of group error compensation techniques. A further remark concerns the γ-type RCs: despite being class 1 devices, they often show ratio errors exceeding 2 %. These values are nonetheless reasonable given the nominal current of 1kA and remain compliant with Table 1001 of the standard [13], which for class 1 sensors specifies a ratio error limit of 3 % at a test current equal to 5 % of the rated primary current, and 1.5 % at 20 % of the rated primary current.

Finally, for all three RC families, the temperature dependence of ratio error is well documented in the literature [47] and has already been addressed by the authors in [48]. Therefore, the discussion is kept focused on the paper's novel contributions.

To further test the authors' hypothesis, the results are evaluated using:

$$\Delta\varepsilon(\%) = |\varepsilon_{T_1} - \varepsilon_{T_2}|\,, \tag{3.15}$$

where ε_T denotes the ratio error at temperature T, and T_1 and T_2 are two setpoints under comparison. Equation (3.15) enables an immediate evaluation of the differing behaviour of the six RCs within each type in terms of ratio error. The outcomes of this evaluation are reported in figure 3.8–figure 3.10 for the α-, β-, and γ-type RCs, respectively.

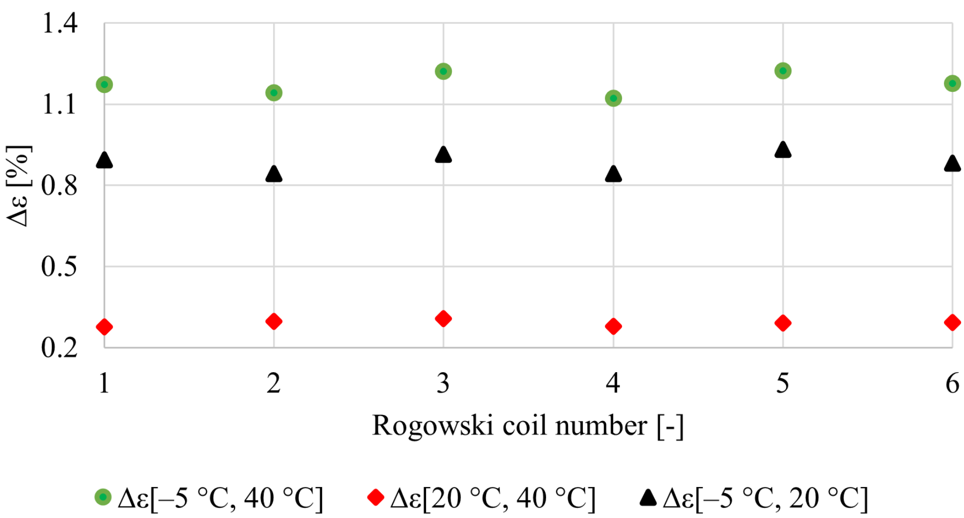

Figure 3.8: Ratio error for each α-type RUT and for test current of 90 A.

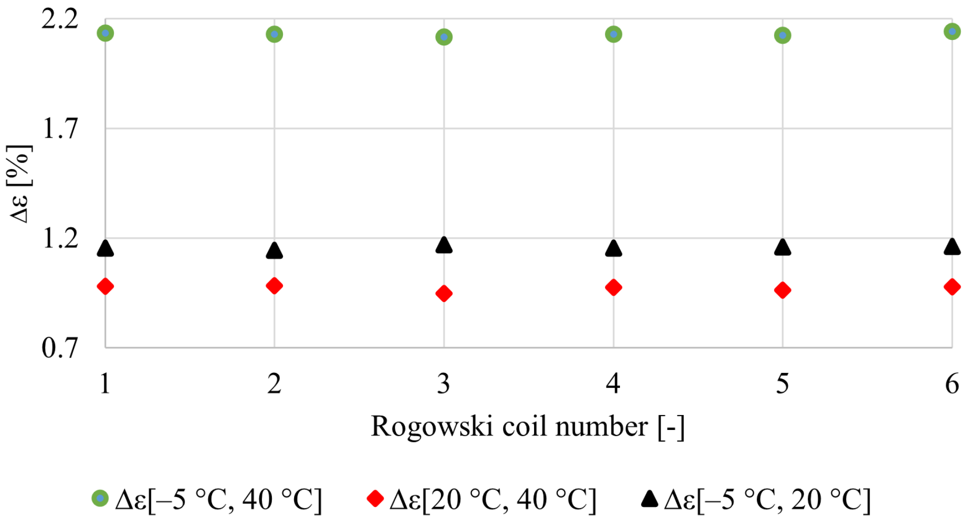

Figure 3.9: Ratio error for each β-type RUT and for test current of 90 A.

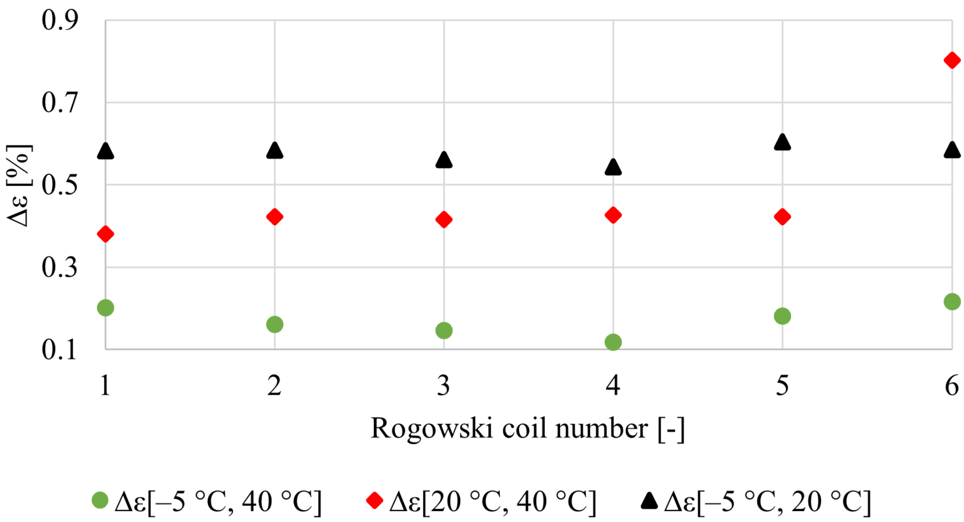

Figure 3.10: Ratio error for each γ-type RUT and for test current of 90 A.

For the α-type (figure 3.8), transitions between temperature setpoints yield a percentage change in ratio error of approximately 9 % among nominally similar devices. This non-negligible spread should be taken into account when performing a compensation technique. In contrast, the β-type (figure 3.9) exhibits a smaller percentage variation temperature-to-temperature of about 2 %; while reduced, this still constitutes an additional uncertainty contribution that can mislead a group-based compensation relative to device-specific adjustment. Finally, the γ-type (figure 3.10) presents the most pronounced behaviour, with percentage variations ranging from roughly 11 % up to 110 %, depending on the device.

In summary, the findings reveal significant variability among the tested devices. In fact, all three types of RCs support the initial hypothesis: temperature excursions induce device-dependent variations in ratio error. This effect is particularly pronounced for the α- and γ-type RCs, highlighting the limitations of group error compensation, that could reduce the accuracy of some IT belonging to the same batch, and the value of individual compensation to ensure optimal performance when accuracy is critical.

3.3 Windowed Sinc for a Simplified Harmonic Characterization of Rogowski Coils under Varying Temperatures with the Monte Carlo Method

The growing need to monitor power systems is driving a substantial increase in the number of measurement points—comprising typically IEDs and ITs. Due to this massive proliferation of sensors, their characterization has become a challenging task for System Operators (SOs) in order to have accurate measurements. In addition, this task must be performed periodically over the years to confirm accuracy and reliability and also the devices must be evaluated under both sinusoidal and distorted conditions making it even more demanding. In conclusion, such characterization processes often become complex, expensive and time-consuming due to the high number of devices installed and the duration of the measurements themselves.

To this end, the primary motivation for this work is to propose and validate a simplified testing procedure for the characterization of RCs frequency response with respect to temperature, without affecting the accuracy of the procedure with respect to traditional characterization methods. Specifically, a comprehensive uncertainty evaluation is performed and the results obtained from the novel method are compared with those of a reference test.

The main advantages of this simplified procedure are: (i) a reduction in testing time and consequently a reduction of cost and (ii) the ability to test a larger number of devices in the same time frame.

Section 3.3 is structured as follows: (i) design of the signal used for the characterization and theory behind the method, (ii) description of measurement setup (iii) performed tests, (iv) uncertainty evaluation, and (v) finally discussion of results and conclusions.

3.3.1 The Novel Approach

The frequency response of a generic IT is conventionally determined using one of the following two main methods. The first technique, known as frequency sweep, involves the sequential application of sinusoidal waveforms, with each signal corresponding to a specific frequency and amplitude of interest. This process yields a precise point-by-point characterization, providing one response value for each frequency and amplitude under investigation. The second technique, known as impulse response, involves the generation of a single impulse signal which is applied to the Device under test (DUT) in order to obtain ideally a frequency characterization across the entire frequency spectrum from a single measurement, as an impulse signal theoretically contains all frequencies. Both characterization methods present distinct and inherent drawbacks that affect their practical application.

- For frequency sweep. The main limitation is its time duration since it is proportional to the number of frequencies to be tested. Consequently, even when the test is automated, this characterization process is inherently more time-consuming than the impulse test.

- For impulse response. The main limitation is the accuracy due to the physical limitations of the hardware used for measurements. Firstly, a power amplifier is incapable of producing an ideal impulse, resulting in a non-constant frequency spectrum that exhibits a roll-off above a certain frequency. This non-ideality limits the available bandwidth. Secondly, the DAQ system must have a sufficiently high sampling frequency to adequately capture the transient nature of the pulse.

Considering these factors, the frequency sweep is often the preferred technique in practice due to its superior reliability, despite being a slower process.

As a potential solution that overcomes the tradeoffs posed by the two legacy methods, this work proposes the use of a well-known signal: the sinc function, thanks to which, with a single measurement and using less sophisticated and performing instrumentation, it is possible to obtain the frequency response of the DUT up to a predefined frequency band. However, designing this waveform requires careful consideration so that the test signal meets both the requirements of a cost-effective characterization process and the use of instrumentation of reduced complexity.

3.3.1.1 Sinc Design

The sinc function is defined as:

$$\mathrm{sinc}(n) = \frac{\sin(K\pi n)}{\pi n}. \tag{3.16}$$

In this formulation, the coefficient K is a parameter derived from three key signal characteristics: (i) the total number of samples N, (ii) the desired frequency range, and (iii) the frequency step. The variable n represents the sample index.

In the frequency domain, the ideal discrete sinc function corresponds to a rectangular spectrum with zero components outside this band. For clarity, the time-domain and frequency-domain representations of this basic function are depicted in figure 3.11 and figure 3.12, respectively. For more details on using the sinc function, [49] presents the theoretical basics behind its design.

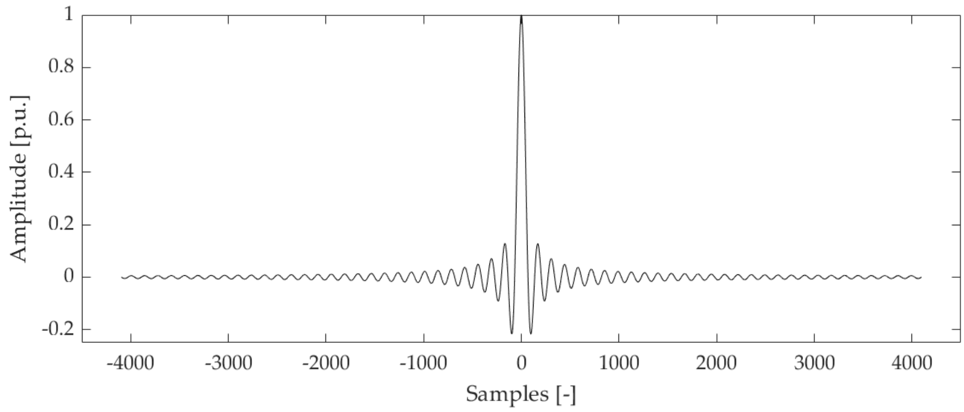

Figure 3.11: Time-domain representation of the sinc function.

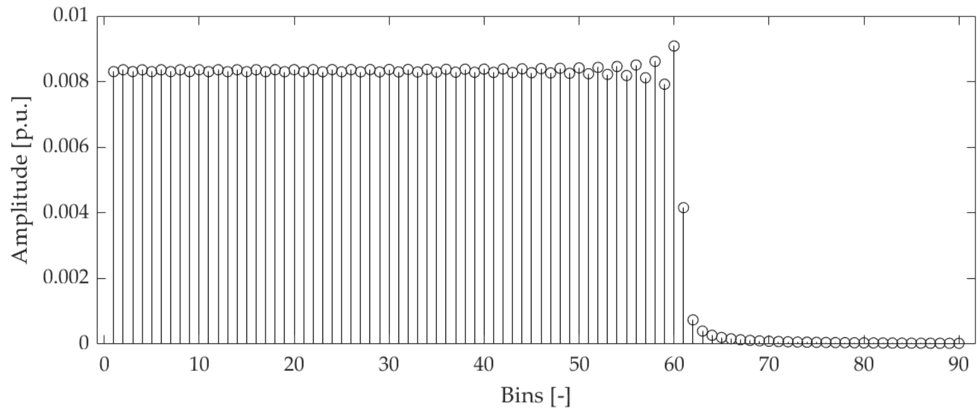

Figure 3.12: Frequency-domain representation of the sinc function.

While this signal has an ideal rectangular spectrum, practical implementation requires modifications to maintain this shape. Therefore, in order to improve the amplitude stability frequency components of the spectrum, a window function is applied to the original sinc waveform. Among all available window functions, the Blackman window is selected in order to reduce the spectral leakage caused by the signal truncation. Since typical Arbitrary Waveform Generators (AWGs) and power amplifiers continuously repeat –concatenate– the waveform saved in its internal memory, this can introduce discontinuities at the boundaries if the signal is not periodic within the window. The Blackman window is defined by:

$$w(n) = 0.42 - 0.5\cos\left(\frac{2\pi n}{N}\right) + 0.08\cos\left(\frac{4\pi n}{N}\right), \tag{3.17}$$

in which all the parameters have been previously described for equation (3.16).

The beneficial effect of applying this window is illustrated in figure 3.13 and figure 3.14, which shows the time- and frequency-domain representations of the Windowed Sinc Function (WSS) (red) superimposed on the original signal (black).

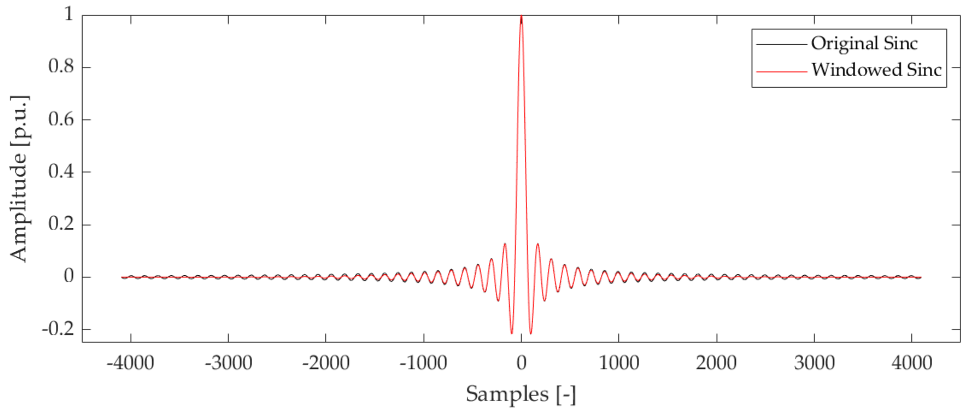

Figure 3.13: Time-domain representation of the WSS.

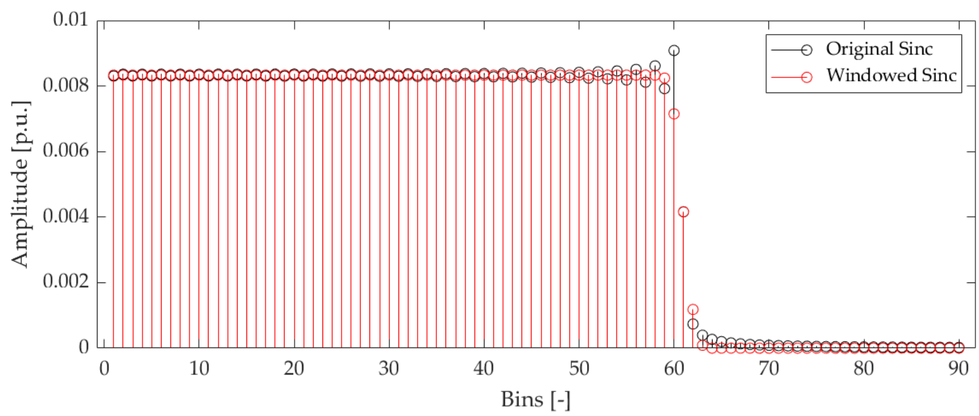

Figure 3.14: Frequency-domain representation of the WSS.

The WSS, which will be used in the following tests, is designed based on three input parameters: (i) the desired frequency resolution equal to 50 Hz, (ii) the cut-off frequency equal to 3000 Hz, and (iii) the maximum number of samples supported by the employed AWG equal to 8192. The frequency resolution is directly determined by the time duration of the WSS –in this case 20 ms–, which corresponds to the signal period configured in the AWG.

3.3.1.2 Sinc Approach

After designing the WSS with the desired frequency range and resolution, the methodology involves applying the WSS to a commercial RC in order to collect its frequency response, also known as Sinc Response (SR), $h(t)$ —similar to an impulse response limited to a portion of the spectrum defined by the operator— hence determine the frequency response of the DUT. Theoretically, the SR encapsulates the RC model. Therefore, knowing of the SR enables the prediction of the RC's output for any arbitrary input signal (obviously within the frequency range defined during the previous WSS design). This reconstruction can be implemented either in the time-domain via convolution or in the frequency domain through the multiplication of the respective spectra. This work adopts the frequency-domain approach. This choice is motivated by the fact that time-domain convolution is a computationally intensive process with significant complexity. Therefore, to minimize the computational burden, the proposed characterization procedure is performed entirely in the frequency domain. The convolution theorem states that the convolution of two arbitrary time-domain signals, $s(t)$ and $h(t)$, is equivalent to the multiplication of their respective spectra in the frequency domain:

$$Y(f) = S(f)\, H(f). \tag{3.18}$$

where $Y(f)$, $S(f)$, and $H(f)$ are the FFT of the DUT output signal $y(t)$, the input signal $s(t)$, and the system's sinc (or impulse) response $h(t)$, respectively. In the context of this work, $h(t)$ is the measured WSS response of the RUT, while $s(t)$ is one the input signal applied to the DUT. In conclusion, by multiplying the spectrum of the known input, $S(f)$, with the transfer function of the RUT, $H(f)$, the resulting spectrum $Y(f)$ provides an estimate of the RC's response to that specific input signal.

A final aspect regarding the proposed characterization procedure is its versatility. In fact, the method does not merely provide a punctual and accurate response; rather, it determines a frequency response $H(f)$, which enables the a-posteriori estimation of the DUT response to any arbitrary input signal.

In light of the above, the aim of this work is to acquire the SR of the same RC at different operating temperatures (20 °C, −5 °C and 40 °C) defined by the standard [14]. Being a single-test characterization method, the SR methodology enables the development of a complete RC harmonic model at each of tested temperatures with just three measurement –one per temperature.

3.3.2 Measurement Setup

During the experimental validation phase, two distinct measurement setups are used. The first uses a common AWG to generate the sinc signal during the proposed test, while the second involves the use of the Fluke calibrator 6105A during the refence test. Figure 3.15 includes both test circuits and for clarity a color-coding scheme is used to distinguish between current and voltage signal paths.

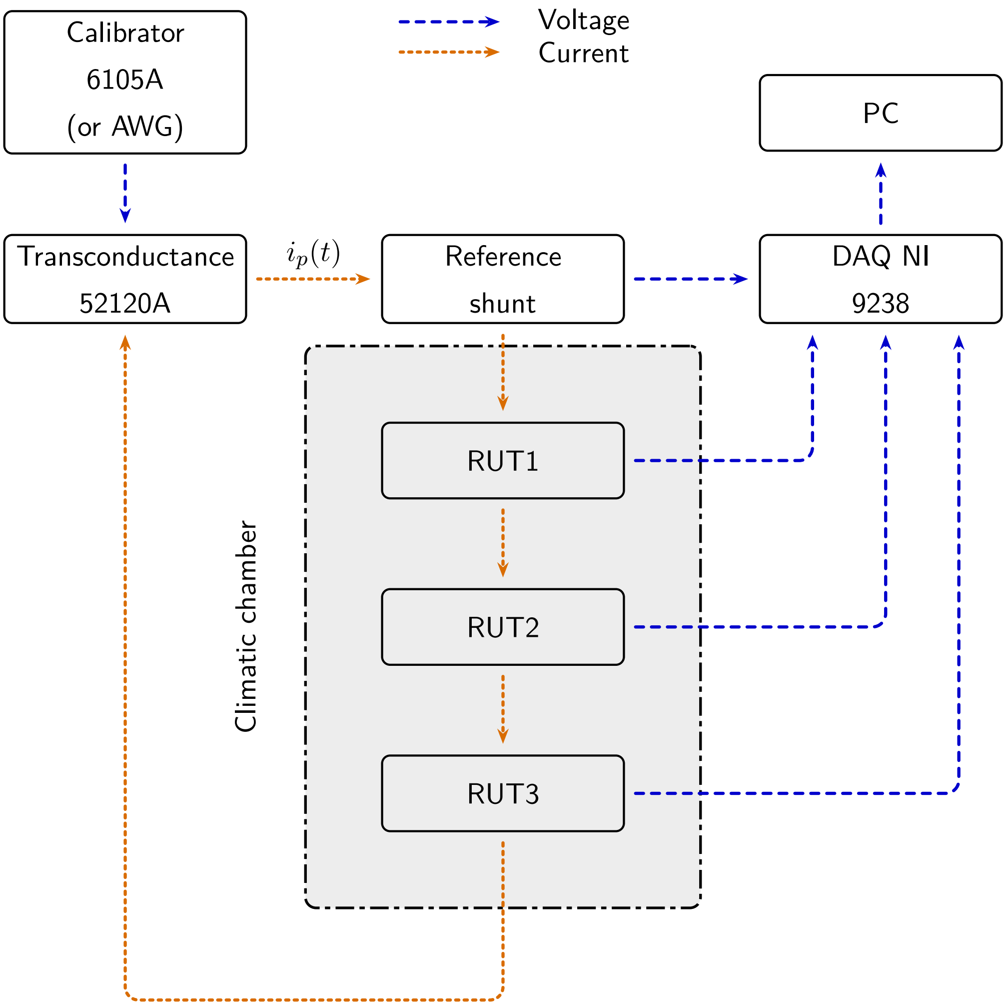

Figure 3.15: Measurement setup with three Rogowski coils inside a climatic chamber.

The experimental setup includes the following components:

- AWG: a Rigol 1022Z and table 3.20 lists the main characteristics;

- Fluke calibrator 6105A;
- Fluke Transconductance 52120A: table 3.21 lists the main characteristics when the device is not controlled by a Fluke calibrator, but rather by other "non-native" devices such as an AWG (as in this work for the proposed test method). This mode is called Stand Alone. On the contrary, table 3.21 lists the main characteristics when the transconductance works together with the calibrator (as in this work for the reference test method);
- NI 9238 and table 3.7 lists the main specifications;
- reference resistive shunt of 1 $m\Omega$ which is characterized in the frequency range of interest in section 3.3.4.1;
- a climatic chamber with an operating temperature range of $-40\,°C$ to $180\,°C$. This device is represented by a grey background hatched block in the block diagram in figure 3.15;
- three commercial RUTs placed inside the climatic chamber;

In brief, depending on the type of test, either the AWG or the Fluke calibrator is used to generate the desired shape of the waveform. Afterwards, the voltage signal is transformed into a current and amplified. This current flows through the test transducers, three commercial RUTs and a reference shunt. Finally, the output of the transducers is collected by the acquisition system controlled in LabVIEW environment.

Table 3.20: Main characteristics of the Rigol 1022Z.

Sampling Frequency	200 MSa/s	**Frequency Resolution**	1 μHz
Frequency Accuracy	$\pm$1 ppm	**Memory**	8192 Sa

3.3.3 Tests Description

Two distinct tests are performed. The first implements the proposed characterization procedure on the RUTs, while the second consisted of implementing a conventional reference method for comparison.

Table 3.21: Main characteristics of Fluke transconductance 52120A for 120 Amp Range case – Stand Alone Mode – Coverage factor k=2.00 (95 % confidence level)

Frequency [Hz]	**% of Output**	**% of Range**	**% Distortion**
10–65	0.012	0.016	0.1
65–300	0.023	0.078	0.1
300–1000	0.078	0.078	0.2
1000–3000	0.233	0.194	0.5

Table 3.22: Main characteristics of the Fluke transconductance 52120A when controlled with a Fluke calibrator for 120 Amp Range – Coverage factor $k = 2.00$ (95 % confidence level).

Frequency [Hz]	**% of Output**	**% of Range**	**Distortion [mA]**
10–850	0.011	0.003	2.5
850–6000	0.052	0.005	39.7

Table 3.23: Main features of the RUTs.

	RUT1	**RUT2**	**RUT3**
Accuracy [%]	±0.5	±1	±1
Output voltage at 50 Hz [mV/kA]	85	100	100
Type	Split core	Split core	Split core
Rated current [A]	1000	–	1000
Inner diameter [mm]	100	120	68

3.3.3.1 Proposed Characterization Method

The objective of this test is to measure the SR of the RUTs. Taking into consideration the measurement setup of figure 3.15, the AWG generates the previous designed WSS of 20 ms-period and therefore the WSS contains multiple harmonics of the 50 Hz fundamental. Afterwards, the created voltage is amplified and converted to current via the transconductance. For each test temperature, a WSS of 100 A peak is injected and then the outputs of the RUTs and the shunt are acquired by the DAQ system. Each record lasts 1 s; consequently, 50 SRs are collected. The sampling frequency of the DAQ board is set to 50 kSa/s.

Similarly to the temperature test of section 3.2, the test temperatures are 20 °C, −5 °C and 40 °C and they are selected according to the RC temperature class reported in the specifications and the standard limits [14]. Preliminary tests were conducted in order to estimate the thermal time constant of the RUTs, indicating that 3 hours were more than enough to reach thermal steady state. The temperature ramp between two setpoints is fixed at $0.1\,°\mathrm{C\,min}^{-1}$. For clarity, figure 3.7 shows the programmed temperature cycle executed by the climatic chamber and in addition they are indicated at the times when the measurements are taken.

3.3.3.2 Reference Method

The chosen reference method is a simple frequency sweep, which requires one measurement for each frequency of interest. Therefore, for each test temperature equal to X, as many measurements must be performed as the selected frequencies equal to Y. Consequently, at the end of the temperature cycle, N measurements equal to $X * Y$ will have been carried out. With an automated system, the total duration is a few minutes; while if human operator is involved, several minutes. In contrast, the SR approach needs only a single 20 ms measurement per temperature to capture the desired portion of the RUT frequency response.

Each reference test used a single-tone sinusoidal waveform at the amplitude specified in table 3.24. For simplicity, only a few frequencies between 50 Hz and 2500 Hz are selected for the reference test, as listed in table 3.24. As in the proposed procedure, a 1 s acquisition window is used and the shunt and RUTs outputs is stored. Once again figure 3.15 illustrates the measurement setup, but this time the calibrator is involved and not the AWG.

3.3.4 Uncertainty evaluation

For an initial assessment of the results and before performing a complete uncertainty evaluation, the typical indices for ITs –the ratio error and the phase displacement– are computed:

Table 3.24: Characteristics of the signals used for the reference tests.

Frequency [Hz]	**Amplitude [A]**
50	100
150	50
250	50
350	50
550	50
650	50
850	50
1250	36
2500	36

$$\Delta\% = \frac{u_E - u_R}{u_R} \times 100 \tag{3.19}$$

$$\Delta\varphi = \varphi_E - \varphi_R \tag{3.20}$$

where u_E and φ_E are the magnitude and phase estimated by the SR method, and u_R and φ_R are those obtained from the reference test. These values are obtained from the FFT of the measured signals. For brevity, the results for RUT 1 are shown in figure 3.16 and figure 3.17 –the ratio error and phase displacement respectively for each tested frequency and temperature.

Two main observations emerge. First, the high level of accuracy achieved across all measurements by the proposed method. In fact, based on table 1.1 which report the limits specified in technical standard [14], the maximum values for the accuracy indices –ratio error and phase displacement– are significantly higher than the values obtained for each harmonic component and in particular the results from the proposed method are up to two orders of magnitude lower than the specified limits. Second, the least favorable performance occurs at 50 Hz. However, as manufacturers and SOs typically already assess their devices at 50 Hz under dedicated operating conditions, adding the 50 Hz fundamental to harmonic testing offers no practical benefit. Hence, when applying the proposed procedure, excluding the 50 Hz component from the

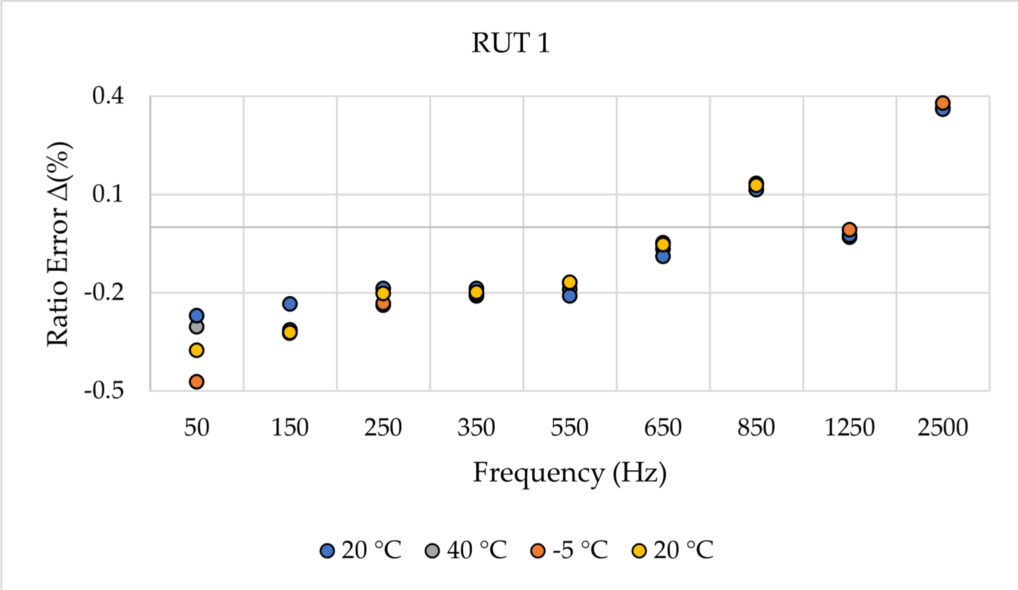

Figure 3.16: Ratio error Δ% for RUT1 for different frequencies and temperature.

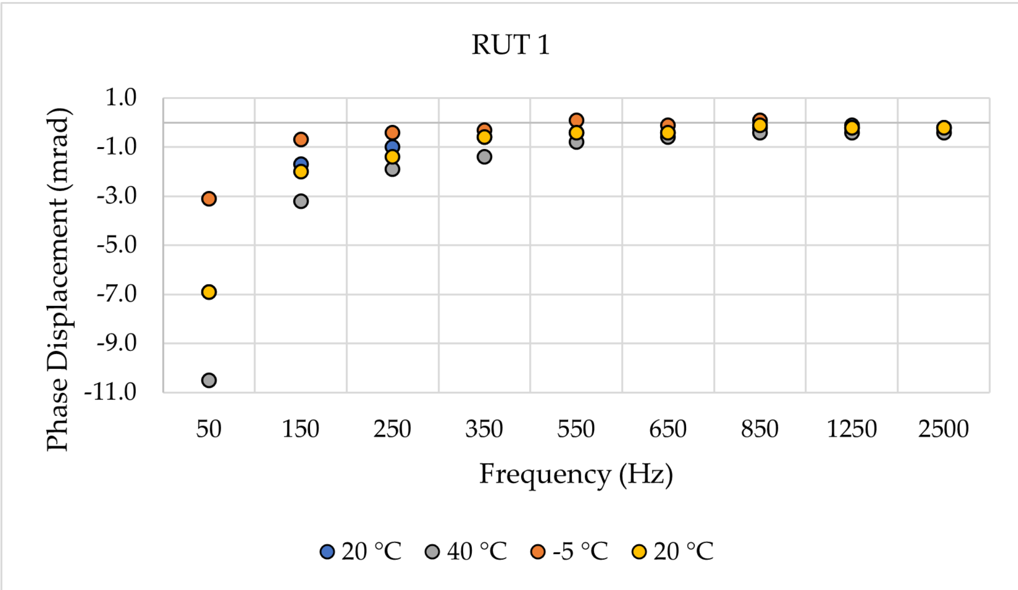

Figure 3.17: Phase displacement $\Delta\varphi$ for RUT1 for different frequencies and temperature.

result evaluation is a reasonable choice. Nevertheless, despite being the least favorable frequency, figure 3.16 and figure 3.17 indicate that, in some cases, the outcomes still comply with the limits set by the relevant standards. In summary, across the three RUTs, the proposed approach enables a clear assessment of their differing performance. Finally, it is important to note the objective of this study is not to judge whether the chosen RUTs perform well at every temperature, but rather to validate the approach itself, irrespective of the absolute magnitude and phase values.

3.3.4.1 Uncertainty Source Analysis

In order to quantify the effectiveness of the proposed characterization procedure, all relevant sources of uncertainty must be identified and rigorously propagated. This process is commonly referred to as ***uncertainty propagation***. The adopted technique is the MCM described in GUM Supplement 1 [19]. In this work, the MCM is applied to both the proposed procedure and the reference test.

To identify the sources of uncertainty, the measurement setup depicted in figure 3.15 must be taken into consideration. Therefore, the DAQ system and the reference shunt resistor are recognized as primary contributors to the uncertainty. To quantify the contribution of these elements, it is necessary to consider table 3.7, which lists the DAQ board accuracy parameters, and table 3.22, which summarizes the performance specifications of the transconductance when controlled by Fluke calibrator as master unit.

Finally, figure 3.18 and figure 3.19 show the characterization of the reference shunt over the frequency range of interest. The first picture represents the amplitude characterization, while the second represents the phase-angle characterization. Specifically, 25 single-tone sinusoidal currents are injected into the shunt at distinct frequencies using the transconductance (controlled by the calibrator). Afterwards, the shunt voltage is measured by the DAQ board. Furthermore, the calibrator employs an additional output signal which is acquired and used as a phase reference to compute the shunt phase displacement. Thus, resistance values and phase displacement versus frequency are obtained from the measured voltage –from the shunt– and the known input current –being set by the operator. As seen in figure 3.18, the amplitude response is essentially flat, whereas figure 3.19 reveals a frequency-dependent phase drift. Finally, this characterization enables the computation of equation (3.21) and consequently the evaluation of the WSS, generated by the transconductance, in the frequency domain.

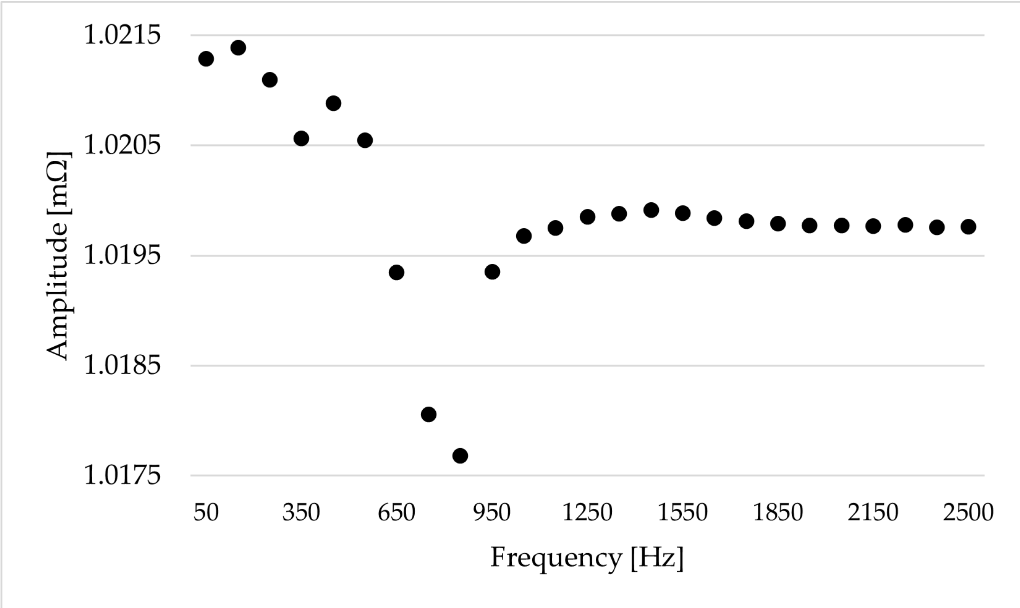

Figure 3.18: Resistance values vs. frequency of the reference shunt resistor.

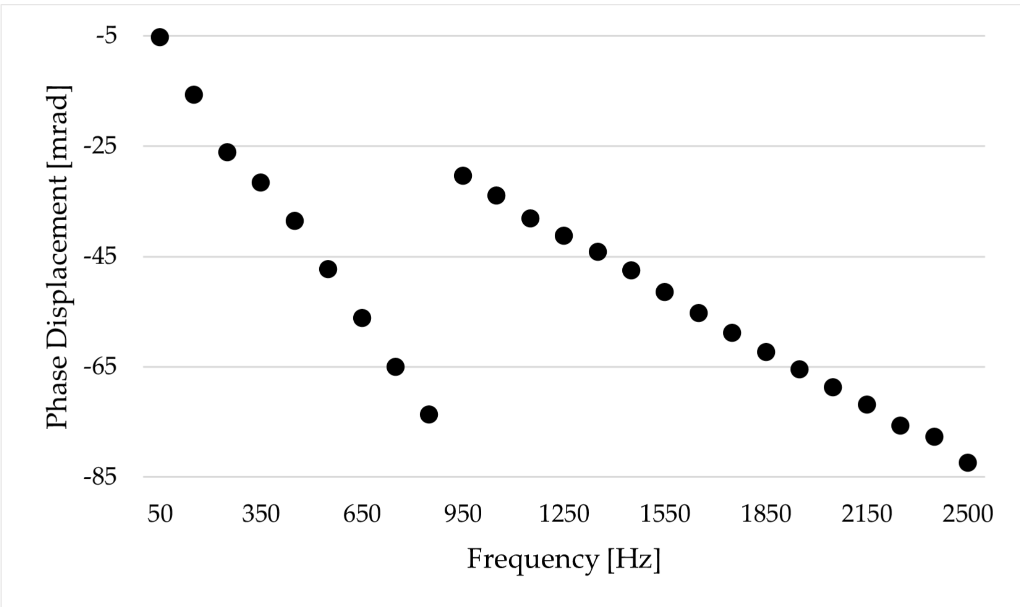

Figure 3.19: Phase displacement vs. frequency of the reference shunt resistor.

3.3.4.2 Monte Carlo Method Application

After defining the uncertainty sources, the MCM can be computed in wich the recorded waveforms are distorted according to instrument accuracy parameters. In particular, the acquired voltage waveforms are perturbed according to the specified instrumentation's accuracy specifications –see table 3.7 and table 3.22. Afterwards, the output voltage and phase displacement of the RUTs are computed for both the proposed method and the reference method, enabling a direct comparison of estimation accuracy of the proposed procedure.

The first stage propagates the uncertainty of the shunt resistor value over the PQ frequency range. Operationally: (i) the primary current –shunt input– is perturbed by the transconductance accuracy parameters, and (ii) the secondary voltage –shunt output– is perturbed by the DAQ board accuracy parameters.

In the second stage, uncertainty propagation continues by perturbing (i) the shunt's secondary voltage using the previously evaluated resistor values (applied to both methods) and (ii) the secondary voltage of the RUTs using the DAQ accuracy parameters. In particular, the shunt's secondary voltage distortion is used for obtaining the distorted primary current according to:

$$\dot{I}_{p,h} = \frac{\dot{V}_{s,h}}{\dot{Z}_h} \tag{3.21}$$

where:

- $\dot{V}_{s,h}$ is the frequency spectrum of the secondary voltage measured from the shunt at the frequency of order h;
- $\dot{Z}_h$ is the value of the shunt resistor at harmonic of order h;
- $\dot{I}_{p,h}$ is the frequency spectrum of the primary current measured thanks to the shunt, which also flows through the RUTs. For the sake of clarity, $\dot{I}_{p,h}$ represents the components of the WSS frequency spectrum implemented in the proposed method. On the contrary, for the reference method, $\dot{I}_{p,h}$ represents the components of the sinusoidal waveforms' frequency spectrum listed in table 3.24. Furthermore, for the latter case, $\dot{I}_{p,h}$ is also the generic input signal $X(f)$ of equation (3.18).

In conclusion, 20000 Monte Carlo iterations are performed. After the application of the FFT, the following quantities from the RUTs are obtained: (i) the output voltage V_{rog}, (ii) the phase displacement $\Delta\varphi_{\text{rog}}$, and (iii) their 95% confidence intervals.

3.3.5 Discussion of the Results

The MCM is used to assess the reliability of the estimates produced by the proposed procedure relative to the reference method. For completeness, the full MCM outputs for RUT 1 are reported in table 3.25 and table 3.26. For each temperature–frequency pair, the tables provide the estimated (Est.) and reference (Ref.) values as the mean and standard deviation computed from the 20,000 Monte Carlo trials. They also report 'Min.' and 'Max.', defined as the lower and upper bounds of the shortest interval containing 95% of the Monte Carlo realizations. Specifically, Table table 3.25 lists the RUT 1 output voltage V_{rog}, while table 3.26 lists the phase displacement $\Delta\varphi_{\mathrm{rog}}$. After the tables, selected results are visualized in a later figure.

Table 3.25: V_{rog} for every temperature, frequency, and signal for RUT 1.

Temp. [°C]	**Freq. [Hz]**	**Signal**	**Min [mV]**	**Mean [mV]**	**Max [mV]**	**Std [mV]**
20	50	Est.	7.095	7.102	7.109	0.004
20	50	Ref.	7.096	7.100	7.105	0.003
20	150	Est.	7.670	7.675	7.680	0.003
20	150	Ref.	7.677	7.681	7.686	0.003
20	250	Est.	7.735	7.740	7.746	0.004
20	250	Ref.	7.745	7.750	7.755	0.004
20	350	Est.	7.725	7.732	7.739	0.004
20	350	Ref.	7.739	7.746	7.753	0.004
20	550	Est.	7.518	7.528	7.537	0.007
20	550	Ref.	7.533	7.545	7.557	0.007
20	650	Est.	7.398	7.409	7.421	0.008
20	650	Ref.	7.417	7.430	7.442	0.008
20	850	Est.	7.099	7.115	7.131	0.010
20	850	Ref.	7.126	7.145	7.164	0.012
20	1250	Est.	5.069	5.360	5.651	0.170

Continued on next page

Table 3.25: V_{rog} for every temperature, frequency, and signal for RUT 1 (cont.).

Temp. [°C]	Freq. [Hz]	Signal	Min [mV]	Mean [mV]	Max [mV]	Std [mV]
20	1250	Ref.	5.046	5.361	5.675	0.200
20	2500	Est.	2.372	2.618	2.864	0.180
20	2500	Ref.	2.000	2.285	2.570	0.200
40	50	Est.	7.152	7.160	7.168	0.005
40	50	Ref.	7.096	7.100	7.105	0.003
40	150	Est.	7.705	7.710	7.714	0.003
40	150	Ref.	7.676	7.681	7.686	0.003
40	250	Est.	7.762	7.767	7.772	0.004
40	250	Ref.	7.744	7.750	7.755	0.004
40	350	Est.	7.739	7.746	7.752	0.004
40	350	Ref.	7.739	7.746	7.753	0.004
40	550	Est.	7.519	7.528	7.538	0.007
40	550	Ref.	7.533	7.545	7.557	0.007
40	650	Est.	7.397	7.408	7.420	0.008
40	650	Ref.	7.416	7.429	7.441	0.008
40	850	Est.	7.092	7.108	7.123	0.010
40	850	Ref.	7.125	7.144	7.163	0.012
40	1250	Est.	5.077	5.373	5.668	0.180
40	1250	Ref.	5.046	5.361	5.675	0.200
40	2500	Est.	2.358	2.608	2.858	0.180
40	2500	Ref.	2.000	2.285	2.570	0.200
−5	50	Est.	7.037	7.045	7.052	0.004
−5	50	Ref.	7.096	7.100	7.105	0.003
−5	150	Est.	7.649	7.653	7.657	0.003
−5	150	Ref.	7.676	7.681	7.686	0.003

Continued on next page

Table 3.25: V_{rog} for every temperature, frequency, and signal for RUT 1 (cont.).

Temp. [°C]	**Freq. [Hz]**	**Signal**	**Min [mV]**	**Mean [mV]**	**Max [mV]**	**Std [mV]**
−5	250	Est.	7.727	7.732	7.737	0.004
−5	250	Ref.	7.744	7.750	7.755	0.004
−5	350	Est.	7.723	7.730	7.737	0.004
−5	350	Ref.	7.739	7.746	7.753	0.004
−5	550	Est.	7.521	7.530	7.538	0.007
−5	550	Ref.	7.532	7.545	7.557	0.007
−5	650	Est.	7.398	7.409	7.420	0.008
−5	650	Ref.	7.416	7.429	7.441	0.008
−5	850	Est.	7.101	7.116	7.132	0.010
−5	850	Ref.	7.126	7.145	7.164	0.012
−5	1250	Est.	5.101	5.411	5.721	0.200
−5	1250	Ref.	5.045	5.338	5.631	0.180
−5	2500	Est.	2.462	2.721	2.979	0.190
−5	2500	Ref.	2.001	2.286	2.570	0.200

Table 3.26: $\Delta\varphi_{\mathrm{rog}}$ for every temperature, frequency, and signal for RUT 1.

Temp. [°C]	**Freq. [Hz]**	**Signal**	**Min [mrad]**	**Mean [mrad]**	**Max [mrad]**	**Std [mrad]**
20	50	Est.	−13.1	−12.4	−11.8	0.3
20	50	Ref.	−5.6	−5.5	−5.4	0.1
20	150	Est.	−18.5	−18.2	−17.9	0.2
20	150	Ref.	−16.7	−16.5	−16.3	0.1
20	250	Est.	−28.9	−28.5	−28.1	0.3
20	250	Ref.	−27.9	−27.5	−27.1	0.3
20	350	Est.	−34.6	−34.2	−33.8	0.3

Continued on next page

Table 3.26: $\Delta\varphi_{\text{rog}}$ for every temperature, frequency, and signal for RUT 1 (cont.).

Temp. [°C]	Freq. [Hz]	Signal	Min [mrad]	Mean [mrad]	Max [mrad]	Std [mrad]
20	350	Ref.	−34.0	−33.6	−33.2	0.3
20	550	Est.	−51.7	−50.9	−50.2	0.5
20	550	Ref.	−51.3	−50.5	−49.8	0.5
20	650	Est.	−61.2	−60.5	−59.7	0.5
20	650	Ref.	−60.8	−60.0	−59.3	0.5
20	850	Est.	−79.6	−78.9	−78.1	0.5
20	850	Ref.	−79.5	−78.7	−78.0	0.5
20	1250	Est.	−54	−49	−44	3
20	1250	Ref.	−54	−49	−44	3
20	2500	Est.	−103	−98	−92	3
20	2500	Ref.	−103	−98	−92	3
40	50	Est.	−16.7	−16.0	−15.4	0.3
40	50	Ref.	−5.6	−5.5	−5.4	0.1
40	150	Est.	−20.0	−19.7	−19.4	0.2
40	150	Ref.	−16.7	−16.5	−16.3	0.1
40	250	Est.	−29.9	−29.5	−29.1	0.3
40	250	Ref.	−28.0	−27.6	−27.2	0.3
40	350	Est.	−35.5	−35.1	−34.6	0.3
40	350	Ref.	−34.0	−33.6	−33.2	0.3
40	550	Est.	−52.1	−51.4	−50.7	0.5
40	550	Ref.	−51.3	−50.6	−49.8	0.5
40	650	Est.	−61.4	−60.7	−60.0	0.5
40	650	Ref.	−60.8	−60.1	−59.3	0.5
40	850	Est.	−79.9	−79.2	−78.4	0.5
40	850	Ref.	−79.5	−78.8	−78.0	0.5

Continued on next page

Table 3.26: $\Delta\varphi_{\mathrm{rog}}$ for every temperature, frequency, and signal for RUT 1 (cont.).

Temp. [°C]	**Freq. [Hz]**	**Signal**	**Min [mrad]**	**Mean [mrad]**	**Max [mrad]**	**Std [mrad]**
40	1250	Est.	−55	−49	−44	3
40	1250	Ref.	−55	−49	−44	3
40	2500	Est.	−103	−98	−93	3
40	2500	Ref.	−103	−98	−92	3
−5	50	Est.	−9.3	−8.6	−7.9	0.3
−5	50	Ref.	−5.6	−5.5	−5.4	0.1
−5	150	Est.	−17.5	−17.2	−16.9	0.2
−5	150	Ref.	−16.7	−16.5	−16.3	0.1
−5	250	Est.	−28.3	−27.9	−27.4	0.3
−5	250	Ref.	−27.9	−27.5	−27.1	0.3
−5	350	Est.	−34.2	−33.8	−33.4	0.3
−5	350	Ref.	−33.9	−33.5	−33.1	0.3
−5	550	Est.	−51.1	−50.4	−49.6	0.5
−5	550	Ref.	−51.2	−50.4	−49.7	0.5
−5	650	Est.	−60.8	−60.1	−59.3	0.5
−5	650	Ref.	−60.7	−60.0	−59.2	0.5
−5	850	Est.	−79.4	−78.6	−77.9	0.5
−5	850	Ref.	−79.4	−78.6	−77.9	0.5
−5	1250	Est.	−54	−49	−43	3
−5	1250	Ref.	−54	−49	−43	3
−5	2500	Est.	−103	−98	−93	3
−5	2500	Ref.	−103	−97	−92	3

The results are reported with a number of significant digits commensurate with the associated standard deviations. Therefore, the initial finding is that the proposed technique is sensitive enough to detect small fluctuations in both amplitude and phase.

For the amplitudes in table 3.25, the confidence intervals obtained with the proposed method overlap those of the reference test at all temperatures and frequencies, confirming the SR approach effectiveness for estimating the output voltage V_{rog} of RUT 1 accurately. Meanwhile, for the phase displacement $\Delta\varphi_{\mathrm{rog}}$ of RC 1, the confidence intervals do not fully overlap with those for tones up to 350 Hz. Overall, the method is consistently valid from 550 to 2500 Hz at all temperatures, whereas in the 50–350 Hz range its effectiveness is temperature-dependent –tending to be less effective at higher temperatures than at lower ones. This behaviour is illustrated in figure 3.20, where blue dots indicate the estimates and red dots indicate the reference values. Only two frequencies (150 and 250 Hz) are shown at three temperatures (20 °C, 40 °C and −5 °C) to emphasize the worst-case scenario. Error bars are barely visible because the 95% confidence intervals are narrow, as also seen in corresponding table 3.26.

The issue of the 50 Hz component has already been discussed in the previous subsection. In any case, the proposed procedure targets harmonic components; hence 50 Hz is included solely for discussion.

Two remarks help interpret the out-of-spec phase-angle values: (i) the instrumentation is highly accurate, yielding very narrow 95% confidence intervals and (ii) the practical significance of harmonic phase angles is limited, as table 1.1 allows broad tolerances. Moreover, the estimates from the proposed method lie well below those limits.

Overall, the SR approach is highly effective and accurate for estimating both the amplitude and phase of the harmonic components considered.

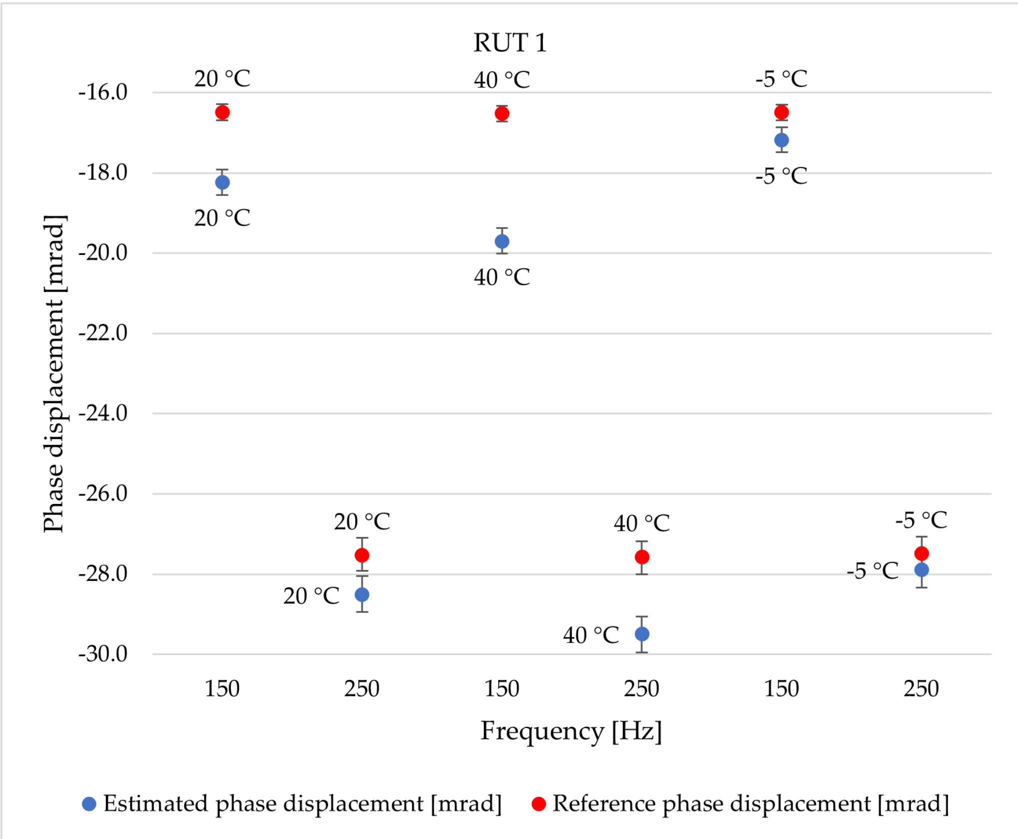

Figure 3.20: $\Delta\varphi_{\text{rog}}$ at 150 Hz and 250 Hz and at tested temperatures for RUT 1.

Conclusions

This thesis presents a line of research activities conducted over three years in the field of electrical measurements applied to challenges of modern power networks. The aim of this work is to advance the state of the art by introducing new insights into the existing literature on the Rogowski coil characterization. The first two chapters establish the theoretical background, followed by the research activities and the main results.

Chapter 1 introduces the fundamentals of current transformers along with a detailed description of the main relevant technologies and all the related standards.

Chapter 2 introduces the concept of measurement uncertainty and the procedures for its calculation.

Finally, the main research is presented in chapter 3, which is divided into three main sections.

The first section validates a new user-friendly frequency model for RCs. The model's simplicity derives from the fact that it relies solely on the parameters available in the RC datasheet. The validity of the proposed modeling approach is evaluated first through simulations and then experimentally on commercial RCs. The results confirm that this simplified model is accurate and readily implementable. Finally, the accuracy of the RC's input-output relationship can be improved with additional information –if available–. Therefore, further studies could pave the way to refine and enhance this model by introducing, for instance, the relationship with temperature.

The second section highlights the limitations of group error compensation techniques applied to RCs –and more generally to any type of ITs–. Experimentally, non-negligible variability has been demonstrated and quantified between nominally identical devices, which can degrade the accuracy of group-based corrections in practice. This behavior is observed in identical RCs of the same manufacturer subjected to the same thermal stress at three temperatures. However, while it is well known that similar devices can exhibit different ratio errors at a fixed temperature, this work shows that the percentage change in ratio error with temperature varies across devices even within the same batch of identical RCs. Therefore, if such variability is ignored, group compensation may yield incorrect adjustments. Such error can be avoided by individual-device compensation. In conclusion, this research emphasizes the need for a conscious selection of compensation strategies in practical applications.

In the third and last section, a new harmonic characterization procedure for RCs is proposed including the impact of temperature. This approach offers clear advantages for both manufacturers and SOs by (i) reducing testing time –and thus cost– and (ii) increasing the number of tested devices within the same time frame– thus increasing the overall productivity. To validate accuracy, the values estimated by the proposed method are compared with those obtained from a reference test. Furthermore, the validation includes a comprehensive uncertainty analysis implementing a MCM –fully compliant with the GUM– in order to assess the overall performance of the sinc approach. The results show that the method is both effective and highly accurate, making it suitable as an all-inclusive procedure to test the accuracy of RCs versus temperature and frequency. Minor limitations in phase-angle estimation are observed but do not materially affect overall performance in the PQ frequency range. Moving forward, further studies could be conducted to assess the sensitivity of the SR approach to additional in-field conditions creating a more realistic scenario. Finally, this work provides a basis for generalizing the method to other types of LPCTs.

List of Figures

List of Tables

List of Acronyms

AC Alternating Current

ADC Analog to Digital Converter

AI Artificial Intelligence

AWG Arbitrary Waveform Generator

BIPM International Bureau of Weights and Measures

CT Current Transformer

CVT Capacitor Voltage Transformers

DAQ Data Acquisition

DC Direct Current

DSO Distribution System Operator

DUT Device under test

EMC Electromagnetic Compatibility

EV Electric Vehicle

FFT Fast Fourier Transform

GUM Guide to the Expression of Uncertainty in Measurement

HV High Voltage

HVDC High Voltage Direct Current

IEC International Electrotechnical Commission

IED Intelligent Electronic Device

IFCC International Federation of Clinical Chemistry and Laboratory Medicine

ILAC International Laboratory Accreditation Cooperation

ISO International Organization for Standardization

IT Instrument Transformer

IUPAC International Union of Pure and Applied Chemistry

IUPAP International Union of Pure and Applied Physics

JCGM Joint Committee for Guides in Metrology

LPCT Low-Power Current Transformer

LPIT Low-Power Instrument Transformer

LPU Law of Propagation of Uncertainty

LPVT Low-Power Voltage Transformer

LV Low Voltage

MCM Monte Carlo method

ML Machine Learning

MV Medium Voltage

NI National Instruments

NMI National Metrology Institute

OIML International Organization of Legal Metrology

PDF Probability Density Function

PE Phase Error

PQ Power Quality

PV Photovoltaic

RC Rogowski Coil

RES Renewable Energy Source

RMS Root Mean Square

RUT Rogowski Under Test

SAMU Stand-Alone Merging Unit

SO System Operator

SR Sinc Response

TC Technical Committee

TF Transfer Function

TR Transformation Ratio

VD Voltage Difference

VIM International Vocabulary of Metrology

VT Voltage Transformer

WB Wideband

WSS Windowed Sinc Function

Bibliography

[1] Y. A. Ahmed, A. Rashid, and M. M. Khurshid. “Investigating the Determinants of the Adoption of Solar Photovoltaic Systems—Citizen’s Perspectives of Two Developing Countries”. In: *Sustainability* (2022). DOI: 10.3390/su141811764.

[2] M. Linhart, V. Rodin, S. Moser, and A. Kollmann. “Citizen Participation to Finance PV Power Plants Focused on Self-Consumption on Company Roofs—Findings from an Austrian Case Study”. In: *Energies* (2021). DOI: 10.3390/en14030738.

[3] V. Breschi, C. Ravazzi, S. Strada, F. Dabbene, and M. Tanelli. “Fostering the Mass Adoption of Electric Vehicles: A Network-Based Approach”. In: *IEEE Transactions on Control of Network Systems* (2022). DOI: 10.1109/TCNS.2022.3164969.

[4] G. Mitsopoulos, V. Kapsalis, A. Tolis, and D. Karamanis. “Innovative Photovoltaic Technologies Aiming to Design Zero-Energy Buildings in Different Climate Conditions”. In: *Applied Sciences* (2024). DOI: 10.3390/app14198950.

[5] R. Monaco, C. Bergaentzle, P. S. Nielsen, and K. Sundsgaard. “Framing barriers for distribution grid digitalisation: A conceptual framework for policy recommendation”. In: *2023 IEEE PES Innovative Smart Grid Technologies - Asia (ISGT Asia)*. 2023. DOI: 10.1109/ISGTAsia54891.2023.10372651.

[6] *Final report of the High-Level Panel of the European Decarbonisation Pathways Initiative*. Publications Office of the European Union, 2018. URL: https://data.europa.eu/doi/10.2777/636.

[7] P. Razmi and M. Ghaemi Asl. “Machine Learning Approaches in a Real Power System and Power Markets”. In: Cham: Springer International Publishing, 2021. DOI: 10.1007/978-3-030-77696-1_17.

[8] Y. Zhu and C. Singh. "End-to-End Topology-Aware Machine Learning for Power System Reliability Assessment". In: *2022 17th International Conference on Probabilistic Methods Applied to Power Systems (PMAPS)*. 2022. DOI: 10.1109/PMAPS53380.2022.9810623.

[9] J.-H. Menke, N. Bornhorst, and M. Braun. "Distribution system monitoring for smart power grids with distributed generation using artificial neural networks". In: *International Journal of Electrical Power & Energy Systems* (2019). DOI: 10.1016/j.ijepes.2019.05.057.

[10] Y. Liu, S. You, W. Yao, Y. Cui, L. Wu, D. Zhou, J. Zhao, H. Liu, and Y. Liu. "A Distribution Level Wide Area Monitoring System for the Electric Power Grid–FNET/GridEye". In: *IEEE Access* (2017). DOI: 10.1109/ACCESS.2017.2666541.

[11] *Instrument transformers - Part 99: Glossary*. IEC 61869-99:2022. Geneva, Switzerland: IEC, 2022.

[12] *International Vocabulary of Metrology — Basic and general concepts and associated terms (VIM)*. JCGM 200:2012 (3rd edition). Joint Committee for Guides in Metrology, 2012. DOI: 10.59161/JCGM200-2012.

[13] *Instrument transformers - Part 10: Additional requirements for low-power passive current transformers*. IEC 61869-10:2017. Geneva, Switzerland: IEC, 2017.

[14] *Instrument transformers - Part 1: General requirements*. IEC 61869-1:2023. Geneva, Switzerland: IEC, 2023.

[15] *Instrument transformers - Part 1: General requirements*. IEC 61869-1:2007. Geneva, Switzerland: IEC, 2007.

[16] *Instrument transformers - Part 6: Additional general requirements for low-power instrument transformers*. IEC 61869-6:2016. Geneva, Switzerland: IEC, 2016.

[17] *Communication networks and systems for power utility automation - ALL PARTS*. IEC 61850:2025 SER. Geneva, Switzerland: IEC, 2025.

[18] *Evaluation of measurement data — Guide to the expression of uncertainty in measurement*. JCGM 100:2008. Joint Committee for Guides in Metrology, 2008. DOI: 10.59161/JCGM100-2008E.

[19] *Evaluation of measurement data — Supplement 1 to the "Guide to the expression of uncertainty in measurement" — Propagation of distributions using a Monte Carlo method*. JCGM 101:2008. Joint Committee for Guides in Metrology, 2008. DOI: 10.59161/JCGM101-2008.

[20] *Instrument transformers - Part 2: Additional requirements for current transformers*. IEC 61869-2:2012. Geneva, Switzerland: IEC, 2012.

[21] *Instrument transformers - Part 3: Additional requirements for inductive voltage transformers*. IEC 61869-3:2011. Geneva, Switzerland: IEC, 2011.

[22] *Instrument transformers - Part 4: Additional requirements for combined transformers*. IEC 61869-4:2013. Geneva, Switzerland: IEC, 2013.

[23] *Instrument transformers - Part 5: Additional requirements for capacitor voltage transformers*. IEC 61869-5:2011. Geneva, Switzerland: IEC, 2011.

[24] *Instrument transformers - Part 9: Digital interface for instrument transformers*. IEC 61869-9:2016. Geneva, Switzerland: IEC, 2016.

[25] *Instrument transformers - Part 11: Additional requirements for low power passive voltage transformers*. IEC 61869-11:2017. Geneva, Switzerland: IEC, 2017.

[26] *Instrument transformers - Part 13: Stand-alone merging unit (SAMU)*. IEC 61869-13:2021. Geneva, Switzerland: IEC, 2021.

[27] *Instrument transformers - Part 14: Additional requirements for current transformers for DC applications*. IEC 61869-14:2018. Geneva, Switzerland: IEC, 2018.

[28] *Instrument transformers - Part 15: Additional requirements for voltage transformers for DC applications*. IEC 61869-15:2018. Geneva, Switzerland: IEC, 2018.

[29] *Instrument transformers - Part 20: Safety requirements of instrument transformers for high voltage applications*. IEC 61869-20:2025. Geneva, Switzerland: IEC, 2025.

[30] *Instrument transformers - Part 100: Guidance for application of current transformers in power system protection*. IEC TR 61869-100:2017. Geneva, Switzerland: IEC, 2017.

[31] *Instrument transformers - Part 102: Ferroresonance oscillations in substations with inductive voltage transformers*. IEC TR 61869-102:2014. Geneva, Switzerland: IEC, 2014.

[32] *Instrument transformers - The use of instrument transformers for power quality measurement*. IEC TR 61869-103:2012. Geneva, Switzerland: IEC, 2012.

[33] *Evaluation of measurement data — Supplement 2 to the "Guide to the expression of uncertainty in measurement" — Extension to any number of output quantities*. JCGM 102:2011. Joint Committee for Guides in Metrology, 2011. DOI: 10.59161/jcgm102-2011.

[34] *Evaluation of measurement data — The role of measurement uncertainty in conformity assessment*. JCGM 106:2012. Joint Committee for Guides in Metrology, 2012. DOI: 10.59161/jcgm106-2012.

[35] *Guide to the expression of uncertainty in measurement — Part 6: Developing and using measurement models*. JCGM GUM-6:2020. Joint Committee for Guides in Metrology, 2020. DOI: 10.59161/jcgmgum-6-2020.

[36] *Guide to the expression of uncertainty in measurement — Part 1: Introduction*. JCGM GUM-1:2023. Joint Committee for Guides in Metrology, 2023. DOI: 10.59161/jcgmgum-1-2023.

[37] T. Orosz, Z. Á. Tamus, and I. Vajda. "Modeling the high frequency behavior of the Rogowski-coil passive L/r integrator current transducer with analytical and finite element method". In: *2014 49th International Universities Power Engineering Conference (UPEC)*. 2014. DOI: 10.1109/UPEC.2014.6934663.

[38] N. Sabiha and H. Alkhammash. "Modeling Rogowski Coils for Monitoring Surge Arrester Discharge Currents". In: *Computer Systems Science and Engineering* (2022). DOI: 10.32604/csse.2022.022506.

[39] X. Liu, H. Huang, and C. Jiao. "Modeling and Analyzing the Mutual Inductance of Rogowski Coils of Arbitrary Skeleton". In: *Sensors* (2019). DOI: 10.3390/s19153397.

[40] J. S. Rodriguez Estupinán, A. Vachoux, and J. Pascal. "Electro-thermal modeling of a Rogowski coil sensor system". In: *VLSI Design, Automation and Test (VLSI-DAT)*. 2015. DOI: 10.1109/VLSI-DAT.2015.7114509.

[41] M. E. Ibrahim and A. M. Abd-Elhady. “Design and Modeling of a Two-Winding Rogowski Coil Sensor for Measuring Three-Phase Currents of a Motor Fed Through a Three-Core Cable”. In: *IEEE Sensors Journal* (2021). DOI: 10.1109/JSEN.2020.3045373.

[42] A. Mingotti, L. Peretto, and R. Tinarelli. “A Simple Modelling Procedure of Rogowski Coil for Power Systems Applications”. In: *2019 IEEE 10th International Workshop on Applied Measurements for Power Systems (AMPS)*. 2019. DOI: 10.1109/AMPS.2019.8897786.

[43] J. Hlavacek, R. Prochazka, K. Draxler, and V. Kvasnicka. “The Rogowski coil design software”. In: *16th IMEKO TC4 Int. Symp. / 13th TC21 Int. Workshop on ADC Modelling and Testing, Proc.* 2008.

[44] M. V. R. Moreno, G. Robles, R. Albarracín, J. A. Rey, and J. M. M. Tarifa. “Study on the self-integration of a Rogowski coil used in the measurement of partial discharges pulses”. In: *Electrical Engineering* (2017). DOI: 10.1007/s00202-016-0456-4.

[45] R. Styblíková and K. Draxler. “Design and Calibration of Rogowski Coils”. In: *Power and Energy Workshop, Noordwijk, The Netherlands*. 2011.

[46] *Voltage Characteristics of Electricity Supplied by Public Electricity Networks*. EN 50160:2022 + A1:2025. Brussels, Belgium: CENELEC, 2025.

[47] A. Yablokov, P. Kabakov, and E. Gotovkina. “Investigation of the Current Conversion Error of Rogowski Coil in a Wide Temperature Range”. In: *2022 International Ural Conference on Electrical Power Engineering (UralCon)*. 2022. DOI: 10.1109/UralCon54942.2022.9906763.

[48] A. Mingotti, F. Costa, L. Peretto, and R. Tinarelli. “Accuracy Type Test for Rogowski Coils Subjected to Distorted Signals, Temperature, Humidity, and Position Variations”. In: *Sensors* (2022). DOI: 10.3390/s22041397.

[49] A. Mingotti, L. Peretto, and R. Tinarelli. “Smart Characterization of Rogowski Coils by Using a Synthetized Signal”. In: *Sensors* (2020). DOI: 10.3390/s20123359.

Appendix A

Demonstration of the Rogowski Coil Input-Output Relationship

This appendix derives the relationship between the unknown current $i(t)$ in the primary conductor and the output voltage $u_s(t)$ of the RC. Figure 1.6 represents an air-cored RC encircling a conductor that carries the unknown current $i(t)$.

Define the following parameters:

μ_0 permeability of free space (magnetic constant);

$u_s(t)$ output voltage of the RC;

n number of turns per unit length (turn density) along the toroidal circumference;

A cross-sectional area of the toroid;

α angle between the magnetic field $\vec{H}$ and the path element $\mathrm{d}\vec{l}$ along the integration path Γ.

Applying Ampere's law along the closed path Γ,

$$\oint_\Gamma \vec{H} \cdot \mathrm{d}\vec{l} = i(t) \qquad \Longleftrightarrow \qquad \oint_\Gamma H \cos\alpha \, \mathrm{d}l = i(t). \tag{A.1}$$

With $\vec{B} = \mu_0 \vec{H}$ and with the surface element linked by the turns $\delta A = A\, n\, \mathrm{d}l$, the elemental linked flux is:

$$\delta\varphi = B\,\delta A = \mu_0\, H \cos\alpha\, A\, n\, \mathrm{d}l. \tag{A.2}$$

Integrating over the entire linked surfaceand recalling equation (A.1) gives:

$$\begin{aligned}\varphi = \iint_A \vec{B} \cdot \hat{n} \, \mathrm{d}A \; &= \; \mu_0 \, A \, n \oint_\Gamma H \cos\alpha \, \mathrm{d}l \\ &= \mu_0 \, A \, n \, i(t).\end{aligned} \tag{A.3}$$

Applying the Faraday–Neumann–Lenz law:

$$u_s(t) \; = \; -\frac{\mathrm{d}\varphi}{\mathrm{d}t} \; = \; -\,\mu_0 \, A \, n \, \frac{\mathrm{d}i(t)}{\mathrm{d}t}. \tag{A.4}$$

Defining the mutual inductance of the air-core toroid as $M = \mu_0 A n$, the input–output relationship becomes:

$$u_s(t) \; = \; -\,M \, \frac{\mathrm{d}i(t)}{\mathrm{d}t}. \tag{A.5}$$

Appendix B

Demonstration of the Rogowski Coil Transfer Function

From the analysis of the circuit represented in figure 3.3, the following formulas –voltage source V_s, series impedance Z_a, and shunt admittance Y_b– are obtainable immediately applying circuit theory and the Laplace transform:

$$V_s(s) = s\,M\,I_p(s), \tag{B.1}$$

$$Z_a(s) = R_w + sL, \tag{B.2}$$

$$Y_b(s) = sC + \frac{1}{Z}. \tag{B.3}$$

Therefore, the simplified electrical model of a RC –figure 3.3– is reduced to the equivalent circuit represented in figure B.1.

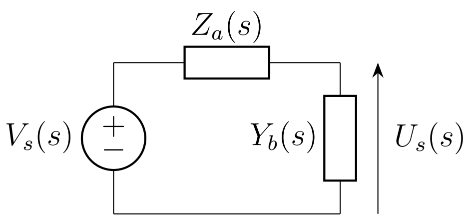

Figure B.1: Schematic of the reduced equivalent circuit of the Rogowski coil.

Subsequently, according to the voltage divider formula, the node voltage U_s can be written as:

$$U_s(s) = \frac{Z_b(s)}{Z_b(s) + Z_a(s)} V_s(s) = \frac{V_s(s)}{1 + Z_a(s) Y_b(s)}. \tag{B.4}$$

Afterwards, equation (B.1) and equation (B.4) are substituted in the following mathematical ratio $\frac{U_s(s)}{I_p(s)}$:

$$\frac{U_s(s)}{I_p(s)} = \frac{s\,M}{1 + \Big(R_w + sL\Big)\Big(sC + \frac{1}{Z}\Big)} = \frac{s\,M}{1 + R_w sC + s^2 LC + \frac{R_w}{Z} + \frac{sL}{Z}}. \tag{B.5}$$

Finally, multiplying numerator and denominator by Z, the desired equation (3.10) representing the TF of the RC:

$$TF(s) = \frac{U_s(s)}{I_p(s)} = \frac{Z\,M\,s}{ZCL\,s^2 + \Big(L + R_w CZ\Big)s + \Big(R_w + Z\Big)}. \tag{B.6}$$

$$\boxed{TF(s) \;=\; \frac{Z\,M\,s}{ZCL\,s^2 + \Big(L + R_w CZ\Big)s + \Big(R_w + Z\Big)}}$$